esa

ECOSPHERE

Forecasting tidal marsh elevation and habitat change through fusion of Earth observations and a process model

Kristin B. Byrd,[1,]† Lisamarie Windham-Myers,[2] Thomas Leeuw,[3,7] Bryan Downing,[4] James T. Morris,[5] and Matthew C. Ferner[6]

[1]*Western Geographic Science Center, U.S. Geological Survey, Menlo Park, California 94025 USA*
[2]*National Research Program, U.S. Geological Survey, Menlo Park, California 94025 USA*
[3]*School of Marine Sciences, University of Maine, Orono, Maine 04469 USA*
[4]*California Water Science Center, U.S. Geological Survey, Sacramento, California 95819 USA*
[5]*Belle W. Baruch Institute for Marine & Coastal Sciences and Department of Biology, University of South Carolina, Columbia, South Carolina 20208 USA*
[6]*San Francisco Bay National Estuarine Research Reserve, San Francisco State University, Tiburon, California 94920 USA*

Citation: Byrd, K. B., L. Windham-Myers, T. Leeuw, B. Downing, J. T. Morris, and M. C. Ferner. 2016. Forecasting tidal marsh elevation and habitat change through fusion of Earth observations and a process model. Ecosphere 7(11):e01582. 10.1002/ecs2.1582

Abstract. Reducing uncertainty in data inputs at relevant spatial scales can improve tidal marsh forecasting models, and their usefulness in coastal climate change adaptation decisions. The Marsh Equilibrium Model (MEM), a one-dimensional mechanistic elevation model, incorporates feedbacks of organic and inorganic inputs to project elevations under sea-level rise scenarios. We tested the feasibility of deriving two key MEM inputs—average annual suspended sediment concentration (SSC) and aboveground peak biomass—from remote sensing data in order to apply MEM across a broader geographic region. We analyzed the precision and representativeness (spatial distribution) of these remote sensing inputs to improve understanding of our study region, a brackish tidal marsh in San Francisco Bay, and to test the applicable spatial extent for coastal modeling. We compared biomass and SSC models derived from Landsat 8, DigitalGlobe WorldView-2, and hyperspectral airborne imagery. Landsat 8-derived inputs were evaluated in a MEM sensitivity analysis. Biomass models were comparable although peak biomass from Landsat 8 best matched field-measured values. The Portable Remote Imaging Spectrometer SSC model was most accurate, although a Landsat 8 time series provided annual average SSC estimates. Landsat 8-measured peak biomass values were randomly distributed, and annual average SSC (30 mg/L) was well represented in the main channels (IQR: 29–32 mg/L), illustrating the suitability of these inputs across the model domain. Trend response surface analysis identified significant diversion between field and remote sensing-based model runs at 60 yr due to model sensitivity at the marsh edge (80–140 cm NAVD88), although at 100 yr, elevation forecasts differed less than 10 cm across 97% of the marsh surface (150–200 cm NAVD88). Results demonstrate the utility of Landsat 8 for landscape-scale tidal marsh elevation projections due to its comparable performance with the other sensors, temporal frequency, and cost. Integration of remote sensing data with MEM should advance regional projections of marsh vegetation change by better parameterizing MEM inputs spatially. Improving information for coastal modeling will support planning for ecosystem services, including habitat, carbon storage, and flood protection.

Key words: biomass; coastal management; elevation; hyperspectral remote sensing; marsh accretion; multispectral remote sensing; sea-level rise; suspended sediment concentration; tidal marsh.

Received 9 September 2016; accepted 23 September 2016. Corresponding Editor: Debra P. C. Peters.

[7] Present address: Sequoia Scientific, Inc., Bellevue, Washington 98005 USA.

† **E-mail:** kbyrd@usgs.gov

Introduction

Management need

The recent Fifth Assessment Report of the Intergovernmental Panel on Climate Change (Church et al. 2013) provides new, increased projections for global mean sea-level rise (SLR) by 2100 based on a range of mechanistic scenarios. Sea-level change along the coast likely will have a strong regional pattern due in particular to differences in vertical land motion (Burkett and Davidson 2012). Thus, SLR will be most effectively projected at regional scales, and its impacts most evident at the state and local levels. At these scales, the impacts of climate change and the associated economic costs of lost productivity, damaged infrastructure, and increasing emergency response costs become more apparent. In addition, SLR could result in the loss of tidal wetlands, with rates and extent of loss varying both in space and time (Thorne et al. 2014). Tidal marshes positively affect wave attenuation and shoreline stabilization (Shepard et al. 2011) and provide natural defense against coastal flooding (Temmerman et al. 2013). Tidal marshes provide habitat for hundreds of fish and wildlife species (Batzer and Baldwin 2012), and tidal marsh soil carbon accretion may average over 200 g $C \cdot m^{-2} \cdot yr^{-1}$ (though varies widely) (McLeod et al. 2011). However, marsh die-off due to SLR could reduce coastal protection from flooding (Temmerman et al. 2012), reduce carbon sequestration potential (McLeod et al. 2011), and lead to extinction and extirpation of resident wildlife populations (Thorne et al. 2012).

Decisions in anticipation of these projected changes, including decisions related to land use planning and development, habitat management, and infrastructure design, are commonly made at the local level (Whitely Binder et al. 2010). Coastal planners are seeking ways to adapt to and mitigate climate change impacts, but managing future risks is complicated by uncertainty in the distribution and extent of these impacts and by the long time horizons over which they may occur (Tompkins et al. 2008). To address the uncertainty in future effects of climate change on coastal ecosystems, new regional planning documents are calling for the use of scenario planning and forecast models. For example, the 2013 Delta Plan for the Sacramento–San Joaquin Delta and Suisun Marsh in California (California Water Code Section 85054) calls for "the development of landscape-scale conceptual models to guide habitat restoration and for modeling future scenarios and predicting system-wide responses using interdisciplinary teams." However, models for most areas do not exist due to lack of sufficient data (Thorne et al. 2015).

One organization supporting coastal adaptive management is NOAA's National Estuarine Research Reserve System (NERRS), a network of 28 reserves distributed around the United States coastline. These reserves serve as regional reference sites to assist local communities in addressing coastal management issues (Buskey et al. 2015). In recent years, reserve managers and researchers have identified the need to reduce uncertainty in forecast models, particularly for inputs such as suspended sediment concentration (SSC) (Ferner et al., *in press*). As collaborators in this study, NERRS scientists have stated an interest in predicting tidal marsh responses to SLR where access to ground data is difficult; in addition, they would like to shift from analyzing extreme future scenarios, and instead model finer patterns of change in time and space (J. Crooks, *personal communication*, August 2014).

Marsh accretion processes

Efforts to understand tidal marsh elevation and habitat response have been ongoing for almost three decades (e.g., McKee and Patrick 1988, Morris and Haskin 1990, Fagherazzi et al. 2012) with more emphasis on the potential effects of increasing sea level in recent years (Kirwan and Guntenspergen 2012, Kirwan and Megonigal 2013, Morris et al. 2013, Thorne et al. 2014). Historically, tidal marshes formed over the past 6000–8000 years as post-glacial rates of SLR reached lows of 1–2 mm/yr (Stanley and Warne 1994). Many marshes have persisted even as sea level has risen approximately 8 m, with tidal marsh elevations being maintained under both saline and freshwater conditions (Drexler et al. 2009). However, currently projected increases in the rates of relative SLR may surpass potential marsh accretion rates, with potential consequences such as loss of elevation-dependent coastal habitats. As a result, scientists have developed and refined a wide range of empirical and numerical models of tidal marsh evolution over

the past century (see review by Fagherazzi et al. 2012).

One mechanistic model of tidal marsh evolution that has shown applicability across multiple salinities and environmental conditions is the Marsh Equilibrium Model (MEM) (Morris et al. 2002). The Marsh Equilibrium Model is a one-dimensional model that projects change in marsh surface elevation with SLR as a function of in situ biomass production and deposition of suspended sediment. The key outputs are elevation above mean sea level on an annual time step to 100 yr, and associated changes in soil and biomass carbon sequestration (Schile et al. 2014). A main feature of MEM is that it simulates the response and feedbacks of marsh vegetation to relative elevation. Plant productivity varies with relative elevation in a parabolic response across a limited range of the tidal frame, with peak productivity occurring at an optimal mid-elevation point (McKee and Patrick 1988, Morris et al. 2013, Morris 2016). An increase in the rate of SLR may cross a threshold whereby relative elevation becomes sub-optimal for growth and accretion rates are insufficient to maintain elevation, leading to elevation loss (Morris et al. 2002).

The uncertainty in data inputs to coastal forecasting models such as MEM can limit prediction accuracy and as a result the usefulness of models in management and planning (Runting et al. 2013). Consequently, accurate information on baseline conditions of tidal marshes, across the modeling spatial extent, is essential for generating realistic forecasts, as baseline conditions set the starting trajectory of change. Models of tidal marsh elevation response to SLR have been populated with field-derived inputs when run at the site level (Schile et al. 2014, Swanson et al. 2014). In contrast, landscape models, in development since the early 1990s, have been parameterized with organic matter accretion rates derived from dated sediment cores, measurements of suspended sediment concentration (SSC) and biomass at limited representative sites, and use of publically available spatial datasets such as the U.S. Fish and Wildlife Service National Wetlands Inventory (Costanza et al. 1990, Craft et al. 2008, Stralberg et al. 2011). While in situ field data are typically used to calibrate and validate MEM, most field-collected datasets are not feasible at the regional extents over which change is occurring (Goetz and Dubayah 2011). Field measurements are labor intensive, often expensive, and may impact sensitive wetland systems (Zhang et al. 1997). Field data also generate model uncertainty due to lack of representativeness (spatial and temporal variability), as well as sampling error.

Use of remote sensing for coastal modeling

Ecological studies can be limited in their capacity to quantify stressors both spatially and temporally, but linking remote sensing and in situ data with process models can help overcome these limitations (Martinez-Lopez et al. 2015). Satellite remote sensing data provide a repeatable, standardized approach to assess spatial and temporal changes in the functioning of ecosystems (Pettorelli et al. 2014). Also, remote sensing-based model inputs provide the potential for annual updates, without the need for annual intensive field sampling. Synoptic and repeated remote sensing measurements may improve model performance and applicability beyond a range of limited sites, while a rich archive of freely available historical remote sensing data provides the capability for hindcasting. However, particularly for coastal habitats, models have utilized only a limited amount of available information that can be derived from imagery. These have been mainly restricted to the use of land cover classifications or variants of the normalized difference vegetation index (NDVI) (Pickens and King 2014).

Deriving data inputs from remote sensing has the potential to extend the applicability of MEM. Although 18 parameters are used to run MEM, previous sensitivity analyses have shown that once calibrated with soil core profile data to constrain soil dynamics, two inputs have a disproportionate influence on model projections (Morris et al. 2016) and have significant temporal and spatial variability: (1) peak aboveground biomass (hereafter biomass) (Kirwan et al. 2009); and (2) annual average SSC (Weston 2014). Both variables can be derived from satellite data (Nechad et al. 2010, Klemas 2013). Normalized difference vegetation index and other vegetation indices derived from moderate resolution Landsat images have been used to map tidal marsh biomass across the United States (Gross et al. 1987, Zhang et al. 1997, Mishra et al. 2012).

Hyperspectral data such as from the 224 band Airborne Visible/Infrared Imaging Spectrometer (AVIRIS) have the potential to improve biomass mapping (Turpie et al. 2015), although there have been limited applications that mainly relied on vegetation indices (Gonzalez Trilla et al. 2013, Schalles et al. 2013).

The use of remote sensing for observing SSC (or total suspended solids) using empirical or semi-analytical techniques has become a routine technique in ocean color research (Matthews 2011). (In this article, we use the term SSC, the MEM input parameter, rather than the term total suspended solids). If the scattering and absorbing properties of the dominate sediment type are known, the sediment optical properties can be incorporated into a marine reflectance model (Nechad et al. 2010). These semi-analytical models are often based on reflectance from a single red or near-infrared band, making them suitable for a variety of remote sensing platforms.

Satellite remote sensing of natural resources, including wetlands, plays a key role in building the analytic capacity for decision-making (Clare and Creed 2014). An additional consideration when applying satellite data is the need for managers to consider acquisition cost, labor needed for analysis, and the level of error associated with its use (Lu 2006, Lewis et al. 2013). Multiple types of imagery are available for mapping at varying cost, spatial and spectral resolution, and temporal frequency, and each provides different advantages. Therefore, a comparison of sensors available for a given modeling application can be used to evaluate the tradeoffs among these data types.

Objectives

We designed a study at the San Francisco Bay NERR in Suisun Bay, California, to address two questions: (1) How can we use satellite-based data to better understand baseline conditions of peak biomass and SSC in a brackish tidal marsh, given the errors and uncertainties in remote sensing? and (2) How can the spatial and temporal distribution and pattern of these variables help determine the spatial scale to which coastal modeling with MEM is applicable? To address these questions, we tested the feasibility of incorporating satellite-based estimates of these two variables into the one-dimensional MEM to transform it into a spatial model for forecasting coastal marsh elevation and vegetation distributions.

Our approach was to run MEM with remote sensing inputs for the first time and apply resulting elevation projections with SLR across a digital elevation model (DEM). The Marsh Equilibrium Model was selected for this study because it models accretion based on the dynamic feedbacks of organic and inorganic inputs with SLR (Morris et al. 2002), which is needed to more accurately forecast marsh elevation change (Kirwan et al. 2016*a*). The Marsh Equilibrium Model has been validated and is applicable to tidal marshes across a range of salinity and substrate types (mineral and peat soils), including at our study site (Schile et al. 2014). Lastly, multiple MEM input variables that define tidal marsh conditions are amenable to measurement with remote sensing.

In this study, we also determined the most appropriate satellite data source in terms of cost, data access, and accuracy. To accomplish this, we compared 30-m Landsat 8 against 2-m WV2 and hyperspectral airborne sensors. Then, Landsat 8-derived inputs were evaluated in a sensitivity analysis of MEM to understand the sensitivity of the model to these inputs and their feedbacks. Our goal for characterizing baseline conditions with satellite data was to reduce uncertainty in model inputs and enable managers to produce more fine-tuned scenarios of change.

Methods

Study area

This project was conducted at the Solano Land Trust Rush Ranch Open Space Preserve (Rush Ranch), a site in the San Francisco Bay National Estuarine Research Reserve (http://www.sfbaynerr.org). Rush Ranch is a highly diverse brackish tidal marsh in the Suisun Marsh complex of Suisun Bay, which is the largest and most intact brackish tidal marsh system in California (Moyle et al. 2014) (Fig. 1). Suisun Bay is a shallow tidal estuary below the confluence of the Sacramento and San Joaquin rivers, characterized by large horizontal salinity gradients with a mean water depth of 1.25 m (Jones and Monismith 2007). Tides in Suisun Bay are mixed-semi-diurnal with a range of approximately 2 m. Prevailing winds in Suisun Bay are southwest and produce relatively large wind waves when aligned with the

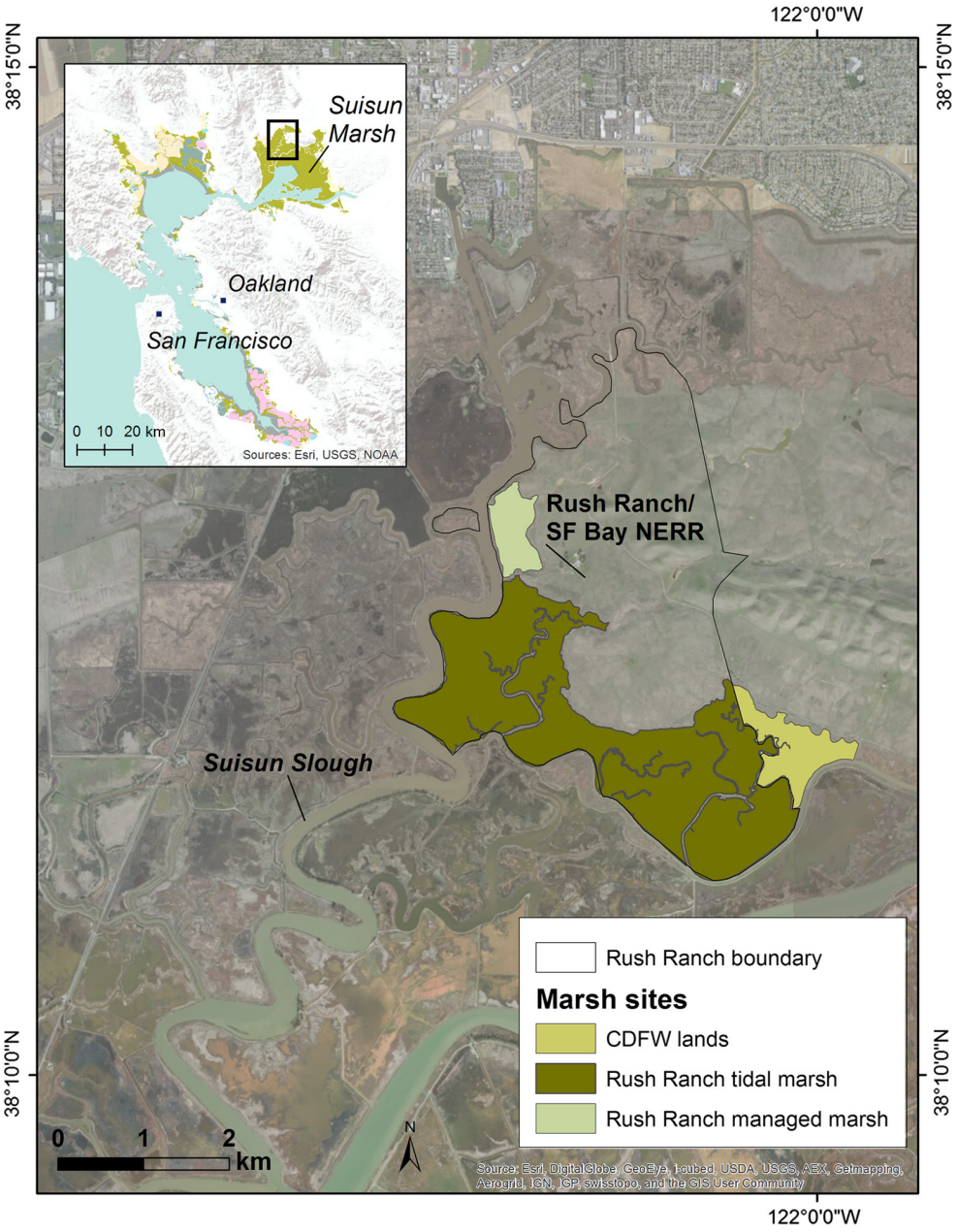

Fig. 1. Study area: Rush Ranch Open Space Preserve (Rush Ranch) and Suisun Slough, Suisun Marsh, California.

approximately 13 km fetch (Warner et al. 2004, Jones and Monismith 2007).

Rush Ranch includes 425 ha of brackish tidal wetlands and a 32-ha diked managed wetland with muted tidal flow. The marsh is composed of plant species distributed according to internal marsh drainage and elevation patterns. The lower intertidal zones along sloughs, or "low marsh habitat," are dominated by California bulrush [*Schoenoplectus californicus* (C.A. Mey.) Palla], hardstem bulrush [*Schoenoplectus acutus* (Muhl. ex Bigelow) Á. Löve and D. Löve var. occidentalis (S. Watson) S.G. Sm.], and cattails (*Typha* spp. L.), all emergent marsh herbaceous

Table 1. Satellite and airborne sensors compared in this study.

Sensor	Sensor type	Spatial resolution (m)	No. of bands	Wavelength range (nm)	Dynamic range (bits)
Landsat 8 OLI	Multispectral satellite	30	8	430–2290	12
WorldView-2	Multispectral satellite	2	8	400–1040	11
AVIRIS	Hyperspectral airborne	16	224	380–2500	16
PRISM	Hyperspectral airborne	3	246	350–1050	14

Note: AVIRIS, Airborne Visible/Infrared Imaging Spectrometer.

species. The higher intertidal zones on the marsh plain or "high marsh habitat" support a range of dominant species that include salt grass [*Distichlis spicata* (L.) E. Greene], Baltic rush (*Juncus balticus* Willd.), three-square bulrush [*Schoenoplectus americanus* (Pers.) Volkart ex Schinz and R. Keller], and pickleweed (*Salicornia pacifica* Standl.) (Grewell et al. 2014, Schile et al. 2014). An invasive plant, perennial pepperweed (*Lepidium latifolium* L.) in the Brassicaceae family, characterized by numerous woody stems and clusters of small, white flowers, has become common in portions of Rush Ranch. Marsh substrate is predominantly highly organic, peat soils including Joice muck and Tamba mucky clay (Soil Survey Staff 2009).

In a previous study in 2011, field data on marsh vegetation, including peak biomass, soils, and elevation, were collected to calibrate MEM for Rush Ranch. No published data on SSC within the marsh were available; therefore, MEM was run for three estimated high, middle, and low concentrations (Schile et al. 2014). Model hindcast of historical vertical accretion rates over the past 100 years was compared to rates calculated using ^{210}Pb dating of six soil cores (Callaway et al. 2012), with model output consistently matching core-based accretion rates (Schile et al. 2014). Subsequently in January 2014, in a second independent study, SSC was measured on the marsh plain of Rush Ranch using siphon samplers at high tide across eight days, along four transects located perpendicular to the marsh channel edges (Ferner et al., *in press*).

Mapping aboveground biomass

During summer 2014, we built empirical models of aboveground biomass of Suisun Marsh emergent vegetation based on satellite reflectance. We evaluated three sensors for mapping biomass: 30-m Landsat 8, 2-m WV2, and 16-m AVIRIS (Table 1).

Biomass field data collection.—Beginning 19 May and continuing through August 8, we sampled aboveground biomass and other ancillary data at Rush Ranch and adjacent marshes, including Hill Slough and Joice Island, which are part of the California Department of Fish and Wildlife Grizzly Island Wildlife Area (Fig. 1). Biomass sampling occurred approximately every 2–3 weeks to capture a wide range in biomass values, and to capture peak biomass that generally occurs in August (Schile et al. 2011). More intensive sampling occurred late May/early June, when AVIRIS flights were planned.

We sampled five to six regularly distributed sample plots in 59 Landsat pixel footprints. Pixel footprints were distributed across dominant plant communities and located along transects perpendicular to channel edges, where peak biomass is typically located (Schile et al. 2011). Plot locations were recorded with a Trimble GeoXT (Sunnyvale, California, USA) sub-meter accuracy global positioning system. At each plot, within a square meter quadrat, we visually estimated percent cover of the top three dominant species, percent cover live and dead vegetation, percent cover bare soil, thatch height, and water depth. We sampled live aboveground biomass within a smaller, 0.1-m^2 quadrat nested in the 1-m^2 quadrat. For two dominant plants, cattail (*Typha* spp.) and hardstem bulrush (*S. acutus*), we estimated biomass with well-established allometric equations (Miller and Fujii 2010, Byrd et al. 2014) to reduce impact to marsh vegetation. For all other plant species, we clipped vegetation to the ground level, separated green vegetation from dead, and then dried green vegetation at 55°C before weighing. All biomass measurements were scaled to a square meter.

Image acquisition and pre-processing.—We downloaded six Landsat 8 scenes from http://earthexplorer.usgs.gov/. We obtained four new

monthly WV2 images of the study region from May through August from the Commercial Imagery-Derived Requirement Tool of the U.S. Geological Survey (https://cidr.cr.usgs.gov/). We downloaded an AVIRIS Level 2 orthocorrected, surface reflection product from the AVIRIS website (http://aviris.jpl.nasa.gov/) flown with NASA's ER-2 aircraft on 28 May 2014 as part of NASA's Hyperspectral Infrared Imager preparatory airborne campaign (http://hyspiri.jpl.nasa.gov/). Of the 224 AVIRIS bands, 20 bands in the water absorption wavelength regions of 1363–1412 nm and 1821–1927 nm were removed due to noise. We atmospherically corrected Landsat 8 and WV2 images using the ENVI atmospheric correction module FLAASH v5.1 (Fast Line-of-sight Atmospheric Analysis of Spectral Hypercubes) with atmosphere settings based on models of the approximate geographic location (ITT Visual Information Solutions 2013). The AVIRIS data were atmospherically corrected according to a modified Atmospheric REMoval algorithm (Green et al. 1998, Thompson et al. 2015). WV2 images were orthocorrected using ENVI's rational polynomial coefficients orthorectification tool and ground control points to achieve a positional accuracy of <1 m. All images were reprojected to meters in UTM Zone 10 WGS 84.

Biomass modeling.—We built two multi date datasets: one from six Landsat scenes and a second from four WV2 scenes. We built a single-date dataset from the AVIRIS scene. For all sensors, reflectance data were matched with biomass data collected on average within 4 d of image acquisition, with a maximum of 14 d between one dataset and a WV2 July image. Biomass values from each plot were attributed to a WV2 pixel. Biomass values from plots located in the same footprint of a Landsat 8 or AVIRIS pixel were averaged, and average biomass values were attributed to reflectance from the corresponding pixel.

For both Landsat 8 and WV2 sensors, we tested the statistical relationships between field measurements, standard indices and simple ratio indices, and two-band vegetation indices (Thenkabail et al. 2004) (Table 2). We also tested the enhanced vegetation index, the wide dynamic range vegetation index (WDRVI), and the soil-adjusted vegetation index due to their success in other remote sensing studies of marsh biomass (Langley and Megonigal 2012, Mishra et al. 2012). The best regression models were established for each sensor. Regression models were run using bootstrap estimation with a resample size of 50, using a total of 50 iterations to measure prediction accuracy. Before data analysis, we log-transformed biomass values in the Landsat 8 dataset and square-root-transformed biomass values in the WV2 dataset to produce normal distributions and minimize the number of outliers.

Table 2. Vegetation indices tested in Landsat 8 and WorldView-2 biomass models.

Index	Formula
Two-band vegetation indices	$TBVI_{ij} = (R_j - R_i)\dagger/(R_j + R_i)$
Simple ratio indices	$SR_{ij} = R_j/R_i$
Enhanced vegetation index	$EVI = [2.5 \times (NIR - R)/(1 + NIR + (6 \times R - 7.5 \times B))]$
Wide dynamic range vegetation index	$WDRVI2 = (0.2 \times NIR - R)/(0.2 \times NIR + R)$ $WDRVI5 = (0.5 \times NIR - R)/(0.5 \times NIR + R)$
Soil-adjusted vegetation index	$SAVI = (NIR - R) \times 1.5)/(NIR + R + 0.5)$

Note: NIR, near-infrared reflectance; *R*, red reflectance.
† R_i and R_j are the reflectance values in bands *i* and *j*.

A portion of Landsat 8 pixels used for model development were located at channel edges and included partial cover of open water. To improve estimation of biomass in these pixels, fraction vegetation cover (FVC) was calculated in ArcGIS 10.2 (ESRI Inc. 1999–2014) using a vector-based vegetation map of Suisun Marsh produced by the California Department of Fish and Wildlife from 2009 high-resolution aerial photography (CDFG 2012). Average biomass values were scaled by FVC for model development. Vegetation indices were tested for a subset of pixels that were fully vegetated and also for the complete dataset with scaled biomass values. For WV2 and AVIRIS datasets, all plots were located within fully vegetated pixel footprints, so no measured biomass values were scaled by FVC.

Partial least squares regression (PLS), a multivariate analysis (Geladi and Kowalski 1986, Mevik and Cederkvist 2004), is a common approach for the analysis of hyperspectral data (Chen et al. 2009, Byrd et al. 2014). For AVIRIS, we used PLS to model aboveground biomass based on canopy reflectance from the 204 AVIRIS bands using the

PLS package in R (Mevik and Wehrens 2007). We minimized model overfitting by selecting the number of components corresponding to the first local minima for root mean square error (RMSE) of prediction, estimated using leave-one-out cross -validation (Mevik and Wehrens 2007).

For all models, we reported the explained variance (R^2), the RMSE (actual vs. predicted biomass measurements), and the per cent normalized RMSE (%RMSE). As the goal of biomass mapping was to estimate peak biomass, for each model we tested the prediction accuracy for high biomass plots by calculating RMSE for plots with biomass values in the top 90th percentile (Byrd et al. 2014).

Biomass maps and pattern analysis.—Biomass maps were generated for an 9 August Landsat 8 image, an 6 August WV2 image, and the 28 May AVIRIS image using the best models from the three sensors. For AVIRIS and Landsat 8, estimated biomass values were scaled to FVC if FVC was greater than 50%. Peak biomass for each map was determined as the maximum biomass value estimated within the tidal marsh at Rush Ranch (Fig. 1). For the Landsat 8 map, we plotted peak biomass values (range: 90th pct. RMSE value to maximum) high-resolution 1-m^2 DEM, which was lidar-derived and vegetation-corrected to surface elevations (NOAA Coastal Services Center 2012, Schile et al. 2014) to assess the relative position of peak biomass within the tidal frame. We also calculated the Global Moran's *I* statistic for spatial autocorrelation (Getis and Ord 1992) in ArcGIS 10.2.2 to determine whether Landsat 8 peak biomass values were dispersed, random, or clustered across the marsh spatial extent.

Mapping suspended sediment concentration

During spring 2014, we built semi-analytical models of SSC for Suisun Bay and adjacent sloughs based on the inherent optical properties of local sediments and satellite reflectance. We evaluated three sensors for mapping SSC: 30-m Landsat 8, 2-m WV2, and 3-m PRISM data (Table 1). PRISM is an airborne hyperspectral sensor designed for aquatic remote sensing in the coastal zone (http://prism.jpl.nasa.gov/prism_data.html).

In situ data collection of SSC and inherent optical properties.—On 5 May 2014, 11 samples of SSC were collected in Suisun Bay and in the neighboring sloughs from 0.5 m below the water surface with a Niskin sampler. The data were collected near the same time as a Landsat 8 scene and a WV2 scene, which were captured approximately an hour and fifteen minutes apart. On 28 April, in coordination with collection of nine PRISM scenes over the Suisun Bay area and the neighboring sloughs, we collected water samples at 12 different stations during the flyover and analyzed them for SSC. Water samples were analyzed in the laboratory using standard filtration methods (APHA 1975, USEPA 1979).

Mass-specific absorption values at six locations near the study site were determined using data collected on 12 March 2014. Absorption from unfiltered water and water filtered with a 0.2-μm filter was measured at nine wavelengths ranging from 412 to 715 nm using an ac-9 (WETLabs, Philomath, Oregon, USA). Water samples for determination of SSC were collected simultaneously. Particulate absorption was calculated by subtracting filtered absorption from unfiltered absorption. Particulate absorption data were scatter-corrected according to Röttgers et al. (2013). The mass-specific absorption was calculated by normalizing the scatter-corrected particulate absorption coefficient by the SSC concentration.

Image acquisition and pre-processing.—For the Landsat 8 image, top of atmosphere reflectances were Rayleigh-corrected using the correction method and Rayleigh optical thickness values from Vanhellemont and Ruddick (2014). Using the Rayleigh-corrected image, the ratio of band 5 (NIR, centered at 865 nm) and band 6 (shortwave infrared [SWIR], centered at 1610 nm) in "clear water" pixels selected several kilometers off the California coast were used to determine the shape of the aerosol reflectance spectrum. These ratios were used to determine the magnitude of aerosol reflectance over the study site for band 5 (Gordon and Wang 1994). The aerosol reflectance was removed from the Rayleigh-corrected image to yield the surface water reflectance.

WV2 scenes were also Rayleigh-corrected according to Vanhellemont and Ruddick (2014). However, the Rayleigh optical thickness and ozone optical thickness were determined by taking the band averages of the Rayleigh and ozone thickness tables from Frohlich and Shaw (1980) and Serdyuchenko et al. (2014), respectively. Due

to lack of SWIR bands, a different aerosol correction, which assumes a constant ratio between two bands (band 7 [NIR1, centered at 833 nm] and band 8 [NIR2, centered at 949 nm]), was used to correct the WV2 scenes as suggested by Ruddick et al. (2000, 2006). PRISM's radiometric data were atmospherically corrected and converted to reflectance using a modified Atmospheric REMoval algorithm (Thompson et al. 2015). For more information, see Fichot et al. (2016).

SSC modeling.—Due to partial cloud cover, seven in situ SSC samples collected at the time of the 5 May Landsat 8 overpass were used to calibrate a single band semi-analytical model of ocean reflectance (Nechad et al. 2010). The Rush Ranch area contains very high concentrations of chromophoric dissolved organic matter (CDOM), which limited the use of the Landsat 8 red band (band 4) (Fichot et al. 2016). Instead, we used the Landsat 8 NIR band (band 5), which is sensitive to SSC scattering (Doxaran et al. 2003).

Mass-specific absorption values were extrapolated from ac-9 measurements using an exponential function (Eq. 1) and was estimated to be 0.0104 m^2/g at 865 nm (absorption per gram at band 5 center). The exponential function had an R^2 of 0.96 and RMSE of 0.0085 m^2/g.

$$a_p^* = 0.089e^{-0.0059(\lambda-500)} \quad (1)$$

The estimated mass-specific absorption at 865 nm was used in the Nechad et al. (2010) single band algorithm. The mass-specific backscattering coefficient was determined by fitting the single band algorithm to the seven SSC-Landsat 8 matchups collected on 5 May to calculate a value of 0.0125 m^2/g at 865 nm. This value falls within the mass-specific scattering values reported in the literature (Neukermans et al. 2012).

A WV2 single band semi-analytical model was developed based on nine SSC in situ data points and reflectance from WV2 band 7 (NIR1, centered at 833 nm). Mass-specific absorption at 833 nm was estimated using Eq. 1. We applied the same value for mass-specific backscattering used in the Landsat 8 model. The dependence of backscattering on wavelength has been observed to be flat near the coast, making this a reasonable assumption (Loisel et al. 2006). A single band semi-analytical model using PRISM reflectance data was developed for wavelength 875 nm with 12 in situ SSC data points. Again, mass-specific absorption was estimated according to Eq. 1 and the same mass-specific backscattering value was applied. For all models, actual vs. predicted SSC values were compared, and RMSE and %RMSE were calculated.

SSC maps and distribution.—Because Landsat 8 has a return interval of 16 d, we used the Landsat 8 SSC model and 12 Landsat 8 scenes (corrected according to methods in section *Image acquisition and pre-processing*) to estimate SSC in Suisun Bay over 12 dates with cloud-free images from June 2013 to May 2014. This time series of SSC enabled us to estimate spatially an annual average SSC, which is the model input parameter for MEM. Using zonal statistics in ArcGIS 10.2, we extracted annual average SSC values from pure water pixels in channels surrounding the Rush Ranch tidal marsh. Pure water pixels were located 30 m from the tidal marsh edge. We quantified the distribution of SSC measured values in the channels using summary statistics interquartile range and standard deviation.

Integration of remote sensing data with the Marsh Equilibrium Model

We tested the integration of the Landsat 8-based inputs of peak biomass and annual average SSC with MEM 3.76 (Morris et al. 2002) and a vegetation distribution model presented in Schile et al. (2014) that defines elevation ranges for four plant communities. Other input parameters came from Schile et al. (2014) (Table 3). The Marsh Equilibrium Model was run at elevations between 0 and 300 cm NAVD88 in 10-cm increments, with projected SLR reaching 1 m after 100 yr, a moderate SLR projection evaluated by Schile et al. (2014). Outputs were mean sea level, marsh elevation, and biomass at yearly time steps from 1 to 100 yr. Following methods of Schile et al. (2014), modeled elevations were applied to the corrected 1-m^2 lidar DEM (NOAA Coastal Services Center 2012). The modeled elevations were then transformed relative to the local tidal datum using the equation: (marsh elevation − mean sea level)/(mean higher high water − mean sea level). We classified the elevations into marsh habitat type based on elevation transitions between mudflat, low marsh, high marsh, and upland vegetation relative to mean sea level according to methods of Schile et al. (2014).

Table 3. Marsh Equilibrium Model field inputs, from Schile et al. (2014).

Variable	Value
Century sea-level rise (cm)	100
Initial rate sea-level rise (cm/yr)	0.24
Mean higher high water (cm NAVD88)	198
Mean sea level (cm NAVD88)	110
Suspended sediment concentration (mg/L)	37†
Marsh elevation (cm NAVD88)	0–300
Max. vegetation elevation (cm NAVD88)	200
Min. vegetation elevation (cm NAVD88)	80
Elevation of peak biomass (cm NAVD88)	170
Max. biomass (g/m^2)	2400
Organic matter decay rate (/yr)	−0.2
Root to shoot ratio (g/g)	3
Refractory carbon fraction, kr (g/g)	0.09
Belowground turnover rate (/yr)	1
Max (95%) root depth (cm)	40
Biomass seasonality	Yes
Trapping coefficient (*ks*, $cm^{-1}{\cdot}yr^{-1}$)	0.0328
Settling velocity (*q*, $g{\cdot}cm^{-3}{\cdot}yr^{-1}$)	0.00146

† Suspended sediment concentration value based on Ferner et al. (*in press*).

Sensitivity analysis

We tested two types of feasibility regarding MEM performance. We compared model outputs derived from remote sensing inputs of peak biomass and annual average SSC and field-measured inputs provided by Schile et al. (2014) and Ferner et al. (*in press*) to assess model sensitivity to the differences between the two. Also, given uncertainties in remote sensing measures, we tested how sensitive the model was to error associated with remote sensing inputs. Model outputs were tested for 80- to 200-cm (marsh edge to upland) initial elevations at 10-cm intervals, at a single magnitude of SLR (100 cm by 2100). The scenarios tested (Table 4) were thus not based on variable SLR but instead on different initial conditions (inputs) for peak biomass and SSC.

The elevation results of model runs (dz/dt) at 10-year intervals were extracted for statistical comparison (n = 10 time points). Response surface modeling was used to generate response curves for each model run that incorporated both elevation and time in the nonlinear surface response. Comparison of response curves were performed by trend response surface analysis of projected elevations under the remote sensing run (Model run no. 1, Table 4) to projected elevations in 11 additional runs (Model run nos. 2–12, Table 4). All analyses were performed with JMP 11 (SAS) statistical software (SAS Institute Inc. 1989–2014). The timestamp at which significant

Table 4. Marsh Equilibrium Model runs for sensitivity analysis of suspended sediment concentration (SSC) and peak biomass inputs, and trend response surface (TRS) statistic and year for model runs no. 2–12 with significant ($*P < 0.05$) deviation from model run no. 1.

Model run no.	Model run	SSC (mg/L)	Peak biomass (g/m^2)	TRS
1	RS†	30	2040	–
2	Field‡	37	2400	0.9431, year 60
3	Field w/RS SSC§	30	2400	0.9395, year 40
4	Field w/RS biomass¶	37	2040	0.9274, year 60
5	RS + RMSE biomass††	30	2366	0.9402, year 60
6	RS − RMSE biomass††	30	1714	ns
7	RS + RMSE SSC‡‡	33.38	2040	0.9461, year 80
8	RS − RMSE SSC‡‡	26.62	2040	ns
9	RS + RMSE biomass, SSC§§	33.38	2366	0.9326, year 60
10	RS − RMSE biomass, SSC§§	26.62	1714	ns
11	RS + RMSE biomass, −RMSE SSC§§	26.62	2366	0.9422, year 60
12	RS − RMSE biomass, +RMSE SSC§§	1714	33.38	0.9424, year 60

Notes: ns, not significant. The TRS statistic is significant if <0.95.
† RS: remote sensing inputs for peak biomass and SSC.
‡ Field: published data as collected by in situ data collection (Schile et al. 2014).
§ Field w/RS SSC: field data for all inputs except the remote sensing SSC.
¶ Field w/RS biomass: field data for all inputs except the remote sensing peak biomass.
†† RS+ or −RMSE biomass: remote sensing peak biomass (±326 g/m^2).
‡‡ RS+ or −RMSE SSC: remote sensing SSC (±3.38 mg/L).
§§ RS+ or −RMSE biomass and RMSE SSC (±3.38 mg/L) and (±326 g/m^2).

Table 5. A comparison of empirical models from Landsat 8 OLI, WorldView-2, and AVIRIS sensors for mapping peak biomass in the Rush Ranch tidal marsh.

Sensor	Model	R^2	n	In situ biomass range (g/m^2)	RMSE (g/m^2)	%RMSE	RMSE 90th pct. (g/m^2)	%RMSE	Max. biomass (g/m^2)
Landsat 8	If FVC >90, log(biomass) ~ WDRVI2	0.56	38	98–1559	227	16	326	71	2040
	If 50 < FVC < 90, log(biomass × FVC) ~ R_{red}/R_{green}	0.57	47						
WorldView-2	Sqrt(biomass) ~ R_{red}/R_{green}	0.22	322	3–2671	408	15	1033	69	1551
AVIRIS	Biomass ~ b1…b204	0.52	46	256–1289	172	17	302	94	1770

Notes: Landsat 8 and WorldView-2 models were based on linear regression, and the AVIRIS model was based on partial least squares regression. FVC, fraction vegetation cover; WDRVI2, wide dynamic range vegetation index; R_{red}/R_{green}, simple ratio index with red and green bands; Max. biomass, peak biomass of Rush Ranch tidal marsh vegetation based on maps derived from each sensor; %RMSE, per cent normalized RMSE; RMSE 90th pct., RMSE for validation samples in the 90th percentile of biomass samples; AVIRIS, Airborne Visible/Infrared Imaging Spectrometer.

diversions appeared between response curves (df: 1, 22) associated with each run was identified at $P < 0.05$. Finally, we calculated differences in elevation projections between Model run no. 1 and all other runs for each time point and starting elevation at 10-cm intervals to illustrate deviations between (1) remote sensing and field-based inputs and (2) error associated with remote sensing inputs.

Results

Biomass maps and pattern analysis

Biomass values from 368 measured field plots ranged from 3 to 3021 g/m^2, with a mean of 668 g/m^2. The biomass distribution was right-skewed, with the top ten plots ranging from 2077 to 3021 g/m^2. When biomass was averaged by 30-m Landsat pixel footprints, biomass values ranged from 98 to 1559 g/m^2. Biomass averaged by AVIRIS pixel footprints ranged from 256 to 1289 g/m^2 (Table 5).

Landsat 8 reflectance data were used to produce a species invariant model of biomass, although one outlier pixel was removed because it was fully dominated by perennial pepperweed, with highly reflective white flowers. Use of the WDRVI2 (NIR reflectance scaled by 0.2) produced the best model for fully vegetated pixels, and best predicted high biomass values in fully vegetated pixels, while the simple ratio index R_{Red}/R_{Green} produced the best model for all pixels including mixed pixels scaled by FVC (Table 5, Fig. 2). As a result, we applied both models and produced a biomass map (Fig. 3A) according to Eq. 2. RMSE for the 90th percentile plots (plots >1100 g/m^2) was 326 g/m^2. When this model was applied to an 8 August Landsat image of Rush Ranch, maximum biomass was estimated to be 2040 g/m^2 within a channel edge pixel. We selected this value as the peak biomass value for the Rush Ranch site.

$$\begin{aligned}&\text{If } \mathrm{FVC} > 90 \text{ then}\\ &\quad \text{biomass} = \exp(5.0 \times \mathrm{WDRVI2} + 7.57) \text{ and}\\ &\text{if } 50 < \mathrm{FVC} < 90 \text{ then}\\ &\quad \text{biomass} = \frac{\exp(-5.29 \times \mathrm{SR}_{red/green} + 12.52)}{\mathrm{FVC}}\end{aligned} \quad (2)$$

The best biomass model based on the WV2 dataset was based on the simple ratio index R_{red}/R_{green} and square-root-transformed biomass (Table 5, Fig. 2). This model also excluded perennial pepperweed plots. RMSE for the 90th percentile plots (plots > 1190 g/m^2) was 1033 g/m^2. The biomass model was applied to an 6 August WV2 image, and maximum biomass at the Rush Ranch tidal marsh was estimated to be 1551 g/m^2.

The PLS regression of AVIRIS bands generated an R^2 of 0.52 and a RMSE of 172 g/m^2. RMSE for the 90th percentile plots (plots >966 g/m^2) was 302 g/m^2. The PLS biomass model was applied to the 28 May AVIRIS image. Maximum biomass at the Rush Ranch tidal marsh was estimated to be 1770 g/m^2. Overall %RMSE of the three models was similar, ranging from 15% to 17%, although %RMSE for high biomass plots was higher for the AVIRIS estimates than for the Landsat 8 or WV2 estimates (Table 5, Fig. 2).

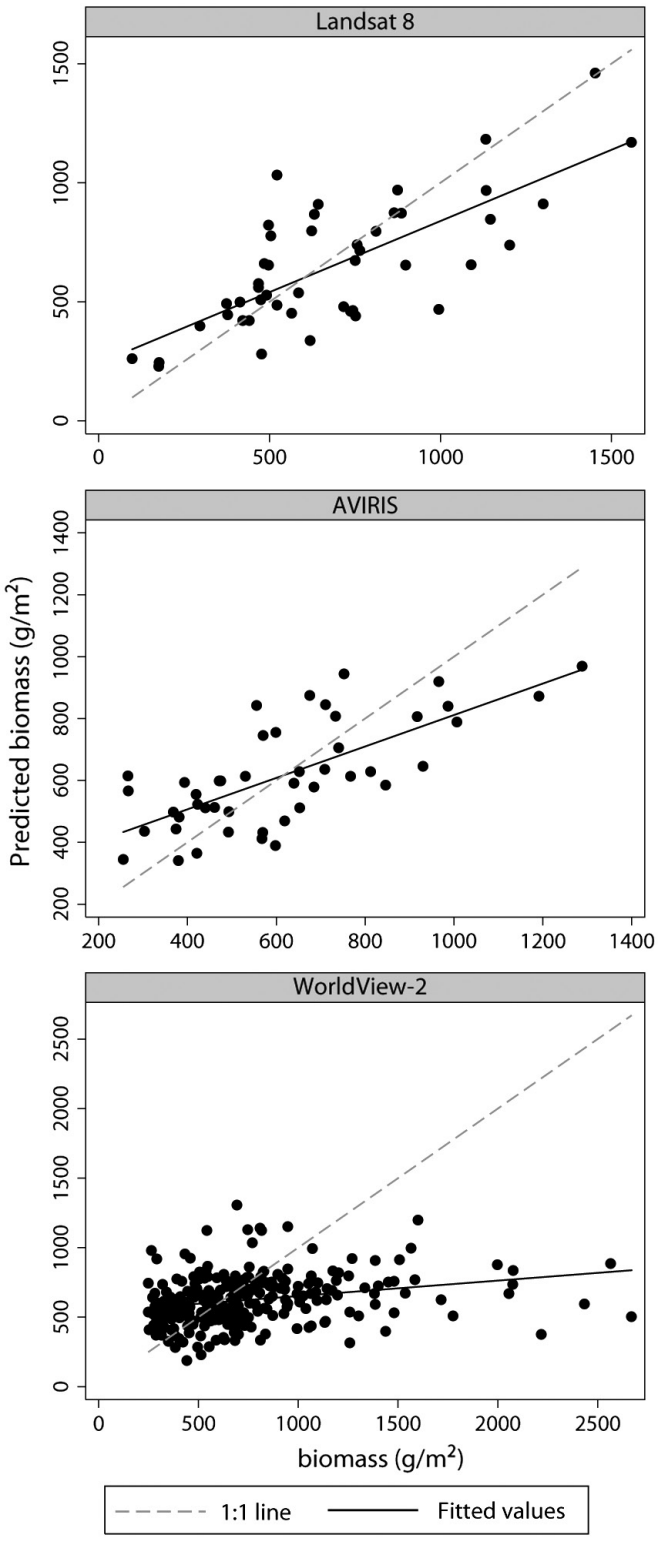

Fig. 2. Plots of actual vs. predicted values of aboveground live biomass based on Landsat 8, Airborne Visible/Infrared Imaging Spectrometer, and WorldView-2 reflectance data and empirical models described in Table 5.

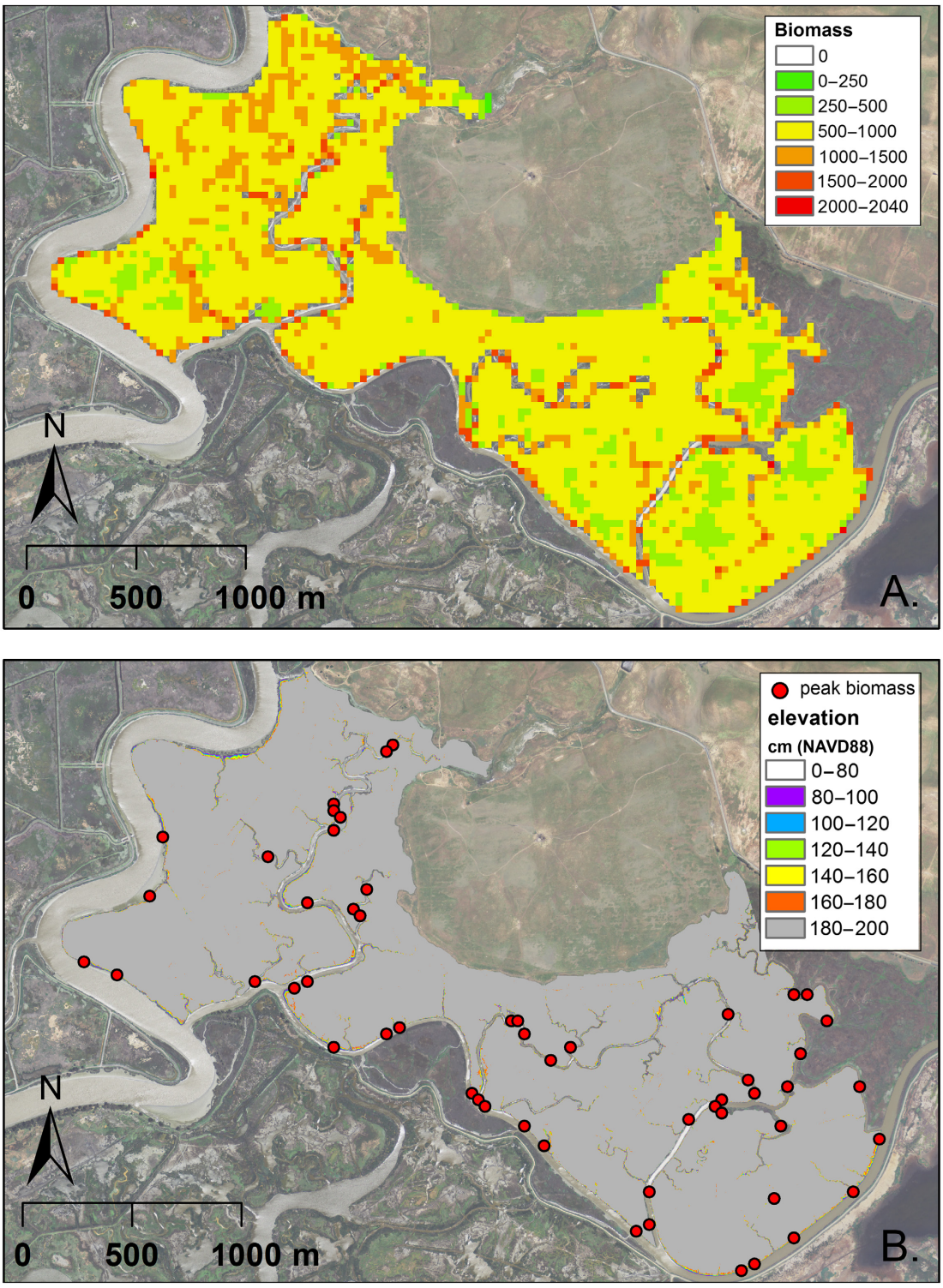

Fig. 3. (A) Map of aboveground live biomass at the Rush Ranch tidal marsh based on Landsat 8 reflectance data. (B) Map of peak biomass values (model RMSE—maximum; 1714–2040 g/m^2) with 1-m^2 corrected lidar-derived digital elevation model.

Table 6. A comparison of single band semi-analytical models developed from Landsat 8 OLI, WorldView-2, and PRISM sensors for mapping suspended sediment concentration in Suisun Bay.

Sensor	Semi-analytical model: SSC (mg/L) =	R^2	RMSE (mg/L)	%RMSE	In situ SSC range (mg/L)
Landsat 8	$1715 \times R_{b5}\dagger/(1 - R_{b5}/0.1179)$	0.66	3.38	22.5	37.8–52.8 ($n = 7$)
WorldView-2	$1271 \times R_{b7}\ddagger/(1 - R_{b7}/0.1080)$	0.45	8.33	23.4	37.8–73.4 ($n = 9$)
PRISM	$1851 \times R_{875}\S/(1 - R_{875}/0.1211)$	0.82	7.28	16.1	23.0–68.3 ($n = 12$)

Note: SSC, suspended sediment concentration.
† R_{b5} = reflectance at band 5 (865 nm).
‡ R_{b7} = reflectance at band 7 (833 nm).
§ R_{875} = reflectance at 875 nm.

All Landsat 8-based peak biomass values were located at the channel edge, at the lower end of the marsh tidal frame (Fig. 3B). Peak biomass distributions were not statistically different than random (Global Moran's *I*: *z*-score = −0.71, *P*-value = 0.48).

Suspended sediment concentration maps and distribution

Based on estimates of mass-specific absorption and scattering, a single band semi-analytical model of SSC was developed for Landsat 8 data with an RMSE of 3.38 mg/L and %RMSE of 22.5% (Table 6, Fig. 4). The final WV2 single band model estimated SSC for nine data points with an RMSE of 8.33 mg/L and %RMSE of 23.4% The final PRISM model estimated SSC with an RMSE of 7.28 mg/L and %RMSE of 16.1% (Table 6, Fig. 4). Based on the Landsat 8 data, we estimated annual average SSC to be 30 mg/L (Fig. 5). Landsat 8-measured SSC values in the channel adjacent to Rush Ranch were normally distributed, with an interquartile range of 29–32 mg/L, standard deviation of 6.1 mg/L, and 80% of values falling between 28 and 33 mg/L (Fig. 6).

To test whether the annual trend in SSC matched the trend in Landsat 8 images, turbidity data from a continuous monitoring station at the study site (http://nerrsdata.org) were matched with reflectance data from the 12 Landsat 8 scenes. Turbidity was converted to SSC using a regional turbidity–SSC relationship ($R^2 = 0.79$; Fleck et al. 2012). Both the in situ turbidity data and the Landsat-derived SSC generated the same seasonal trend in SSC ranging from approximately 20 mg/L in the winter and up to nearly 100 mg/L in the spring.

Marsh Equilibrium Model sensitivity analysis

Comparison of model outputs using field inputs vs. remote sensing inputs.—Model inputs for data sourced from remote sensing products were slightly lower (11–16%) than those collected in the field. Therefore, when observed, deviations in model performance led to slightly lower projected rates of accretion over the 100-year time frame when remote sensing products were used. Trend response surface analysis identified significant diversion ($P < 0.05$) between field and remote sensing-based model runs at 60 yr due to high model sensitivity at the marsh edge (80–140 cm NAVD88; relative starting elevation −0.34 to 0.34; Table 4). However, model performance was insensitive to deviations in peak biomass and SSC across 97% of the marsh plain, initially characterized as high marsh habitat. Even after 100 yr, projected elevations in this dominant marsh zone (150–200 cm NAVD88; relative starting elevation 0.45–1.0) were less than 10 cm different from field-sourced projections (Fig. 7).

Model sensitivity to error in remote sensing estimates.—Figs. 8A and 9H show the difference in MEM-projected elevation along an elevation gradient (*X* axis) and over time (*Y* axis) between two model runs: one using the remote sensing estimates of peak biomass and/or SSC, and one using the remote sensing estimates of peak biomass and/or SSC, plus or minus model RMSE. These figures indicate that from the marsh edge to upland (80–200 cm), biomass variability has a larger influence on elevation projections than suspended sediment variability, starting earlier in the 100-year model run and extending across a greater elevation range (Fig. 8A–D). The most concentrated and significant effects of biomass variability were observed at the marsh edge, whereby over- and underestimates of biomass based on RMSE values led to approximately ±20 cm differences at year 100 (Fig. 8A, C). The greatest difference in elevation projections was found in a comparison between the remote sensing run (Model run no. 1, Table 4)

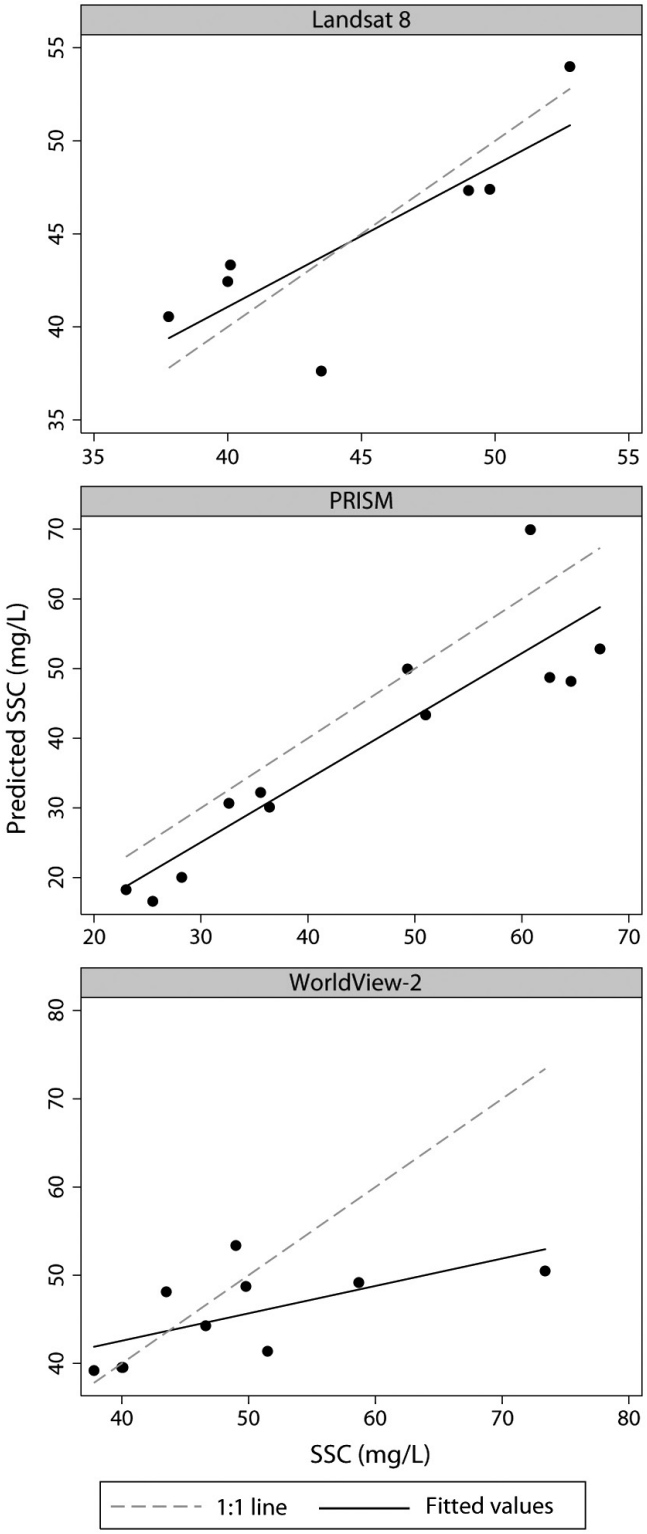

Fig. 4. Plots of actual vs. predicted values of suspended sediment concentration based on Landsat 8, PRISM, and WorldView-2 reflectance data and semi-analytical models described in Table 6.

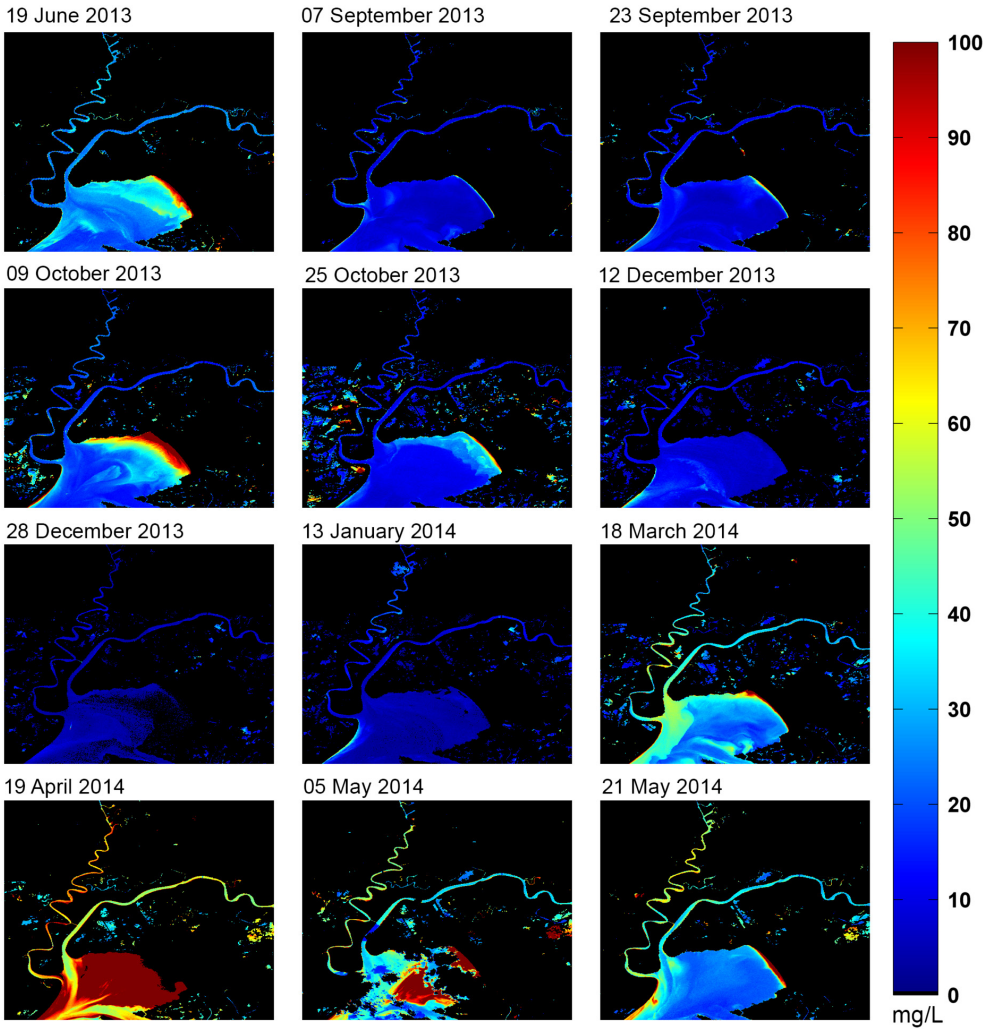

Fig. 5. Time series of estimated suspended sediment concentration (mg/L) in Suisun Bay from June 2013 to May 2014 based on 12 Landsat 8 scenes.

and the RMSE BM-SSC run (Model run no. 10, Table 4), with the latter being 38.7 cm lower at 90 cm at 100 yr (Fig. 8H). However, the trend response surface analysis of these two runs found no significant difference due to lack of significant diversions between response curves across time and initial elevation (Table 4). These results demonstrate that while the trend response surface analysis is most useful for identifying nonlinear diversions between model trajectories, a comparison of elevation projections at specific starting elevation points can reveal where model sensitivity is greatest.

Comparison of field and remote sensing-based vegetation distribution maps.—Both field and remote sensing-based MEM projections, when applied to the corrected Lidar DEM of the tidal marsh, illustrated a subtle "sinking" of the marsh platform to lower in the tidal frame, and projected a change from high marsh habitat to low marsh habitat by 2100. A comparison of plant community maps indicates that the use of field and remote sensing inputs produced the same distributions for mudflat, low marsh, and high marsh at 100 yr (Fig. 9).

Discussion

In this study, we used synoptic measurements of two key variables, peak aboveground biomass

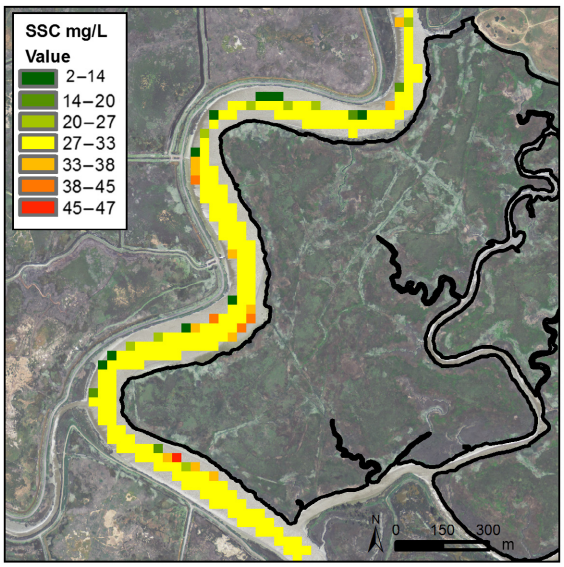

Fig. 6. Map of Landsat 8-measured annual average suspended sediment concentrations in pure water pixels adjacent to Rush Ranch.

and annual average SSC, to improve understanding of baseline tidal marsh conditions that influence ecogeomorphic feedbacks between tidal inundation and vertical accretion across space and time. We analyzed the spatial pattern and distribution of these satellite-based estimates and determined that they represent conditions across the spatial extent of a brackish tidal marsh.

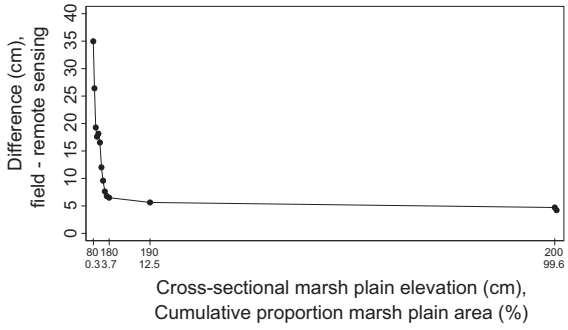

Fig. 7. Difference in Marsh Equilibrium Model elevation projections derived from field-measured inputs and Landsat 8-based inputs as a function of present-day marsh elevation. Differences are plotted along a cross-sectional marsh plain elevation gradient. The cumulative proportion of marsh area along the cross section from channel edge (80 cm) to upland boundary (200 cm) is provided for a subset of elevations.

As a result, the MEM elevation projections based on these estimates should be applicable across this domain. We compared Landsat 8 data to hyperspectral (AVIRIS, PRISM) and high spatial resolution multispectral (WV2) data for mapping biomass and SSC. We determined that Landsat 8 is suitable for this application due to its comparable performance with the other sensors based on model error, its temporal frequency, and data access. Comparison of marsh elevation forecasts from Landsat 8 and field-based inputs to MEM found no significant difference in projections across more than 95% of the marsh plain area at 100 yr, with both projections illustrating a subtle "sinking" loss of elevation of the marsh. This application of remote sensing data improves forecasts of coastal marsh elevations and vegetation distributions across regions relevant to decision-making by reducing uncertainty in input variables both within sites and at the landscape scale.

Because MEM is a dynamic model that accounts for nonlinear feedbacks between increased tidal inundation and increased rates of sediment accretion, it provides more accurate predictions of marsh loss than models that lack these feedbacks and overestimate marsh vulnerability to SLR (Kirwan et al. 2016*a*). However, MEM is an equilibrium model, and changing baseline conditions (e.g., salinity, invasive species) may alter its performance. Increased flooding, subsidence, restricted sediment delivery, and salinity intrusions can lead to many different biogeomorphic feedbacks (e.g., nutrient supply, salinity stress, plant community changes), such that the net effect is less predictable (Kirwan and Megonigal 2013). Despite this uncertainty, hydrodynamic modeling of our study region has shown that vegetation and salinity regimes are likely to not have threshold shifts over the next 50 years (Knowles 2010, Enright et al. 2013), which is the regional planning horizon for the Bay Delta Conservation Plan, a comprehensive conservation strategy for the Sacramento–San Joaquin Delta, including Suisun Marsh (http://baydeltaconservationplan.com/).

Sensor comparison—biomass and SSC

The MEM calls for inputs of peak aboveground biomass. However, the challenge of using NDVI-type indices derived from satellite data for estimating biomass is that they asymptotically

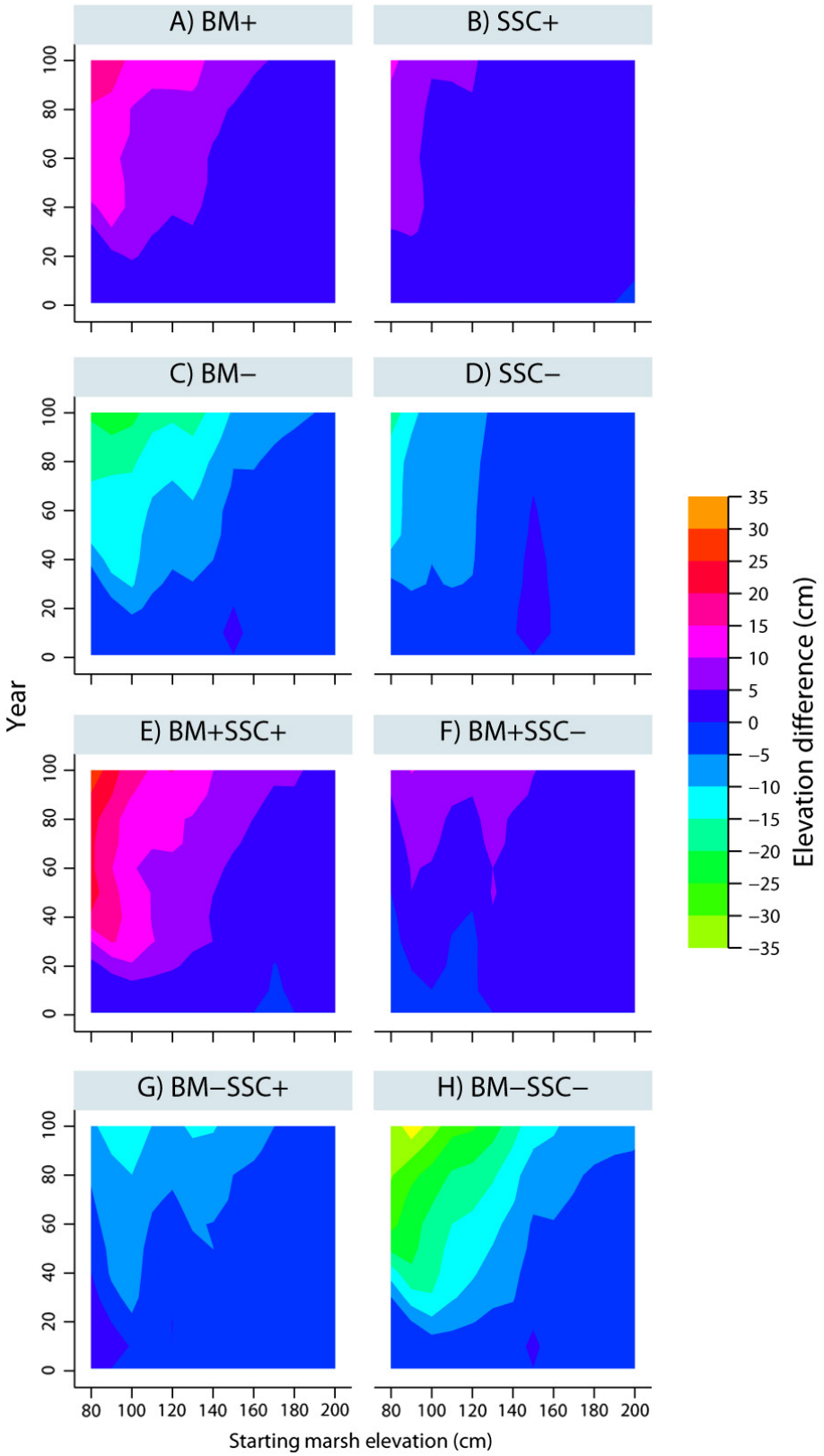
A) BM+
B) SSC+
C) BM−
D) SSC−
E) BM+SSC+
F) BM+SSC−
G) BM−SSC+
H) BM−SSC−
Year
0
20
40
60
80
100
80
100
120
140
160
180
200
Starting marsh elevation (cm)
35
30
25
20
15
10
5
0
−5
−10
−15
−20
−25
−30
−35
Elevation difference (cm)

Fig. 8. The difference in Marsh Equilibrium Model projected elevation along the tidal marsh elevation gradient (cm NAVD88; *X* axis) and over time (0–100 yr; *Y* axis) between two model runs: one based on remote sensing estimates of peak biomass and/or suspended sediment concentration (SSC), and one based on remote sensing estimates of peak biomass and/or SSC, plus or minus model RMSE. (A) (+RMSE biomass) − (RS biomass); (B) (+RMSE SSC) − (RS SSC); (C) (−RMSE biomass) − (RS biomass); (D) (−RMSE SSC) − (RS SSC); (E) (+RMSE biomass, +RMSE SSC) − (RS biomass, RS SSC); (F) (+RMSE biomass, −RMSE SSC) − (RS biomass, RS SSC); (G) (−RMSE biomass, +RMSE SSC) − (RS biomass, RS SSC); (H) (−RMSE biomass, −RMSE SSC) − (RS biomass, RS SSC). See Table 4, Model runs 4–12 for input values.

approach a saturation level at high biomass density (Tucker 1977) and do not estimate biomass well at 100% vegetation cover (Rocchio 2005). In addition, patch size, variable species composition, presence of litter, and water inundation pose challenges when developing biomass maps for wetland vegetation (Byrd et al. 2014). Despite these challenges, our Landsat 8-based hybrid model with WDRVI used for fully vegetated pixels and simple ratio red/green index for mixed pixels sufficiently estimated peak biomass with accuracy needed for the MEM. The WDRVI increases the linearity between biomass and NIR reflectance, thus reducing sensor saturation (Gitelson 2004). The use of a red/green index for pixels with a water signal is appropriate because the ratio of green to red reflectance is close to 1 and avoids water absorption of NIR wavelengths (Motohka et al. 2010).

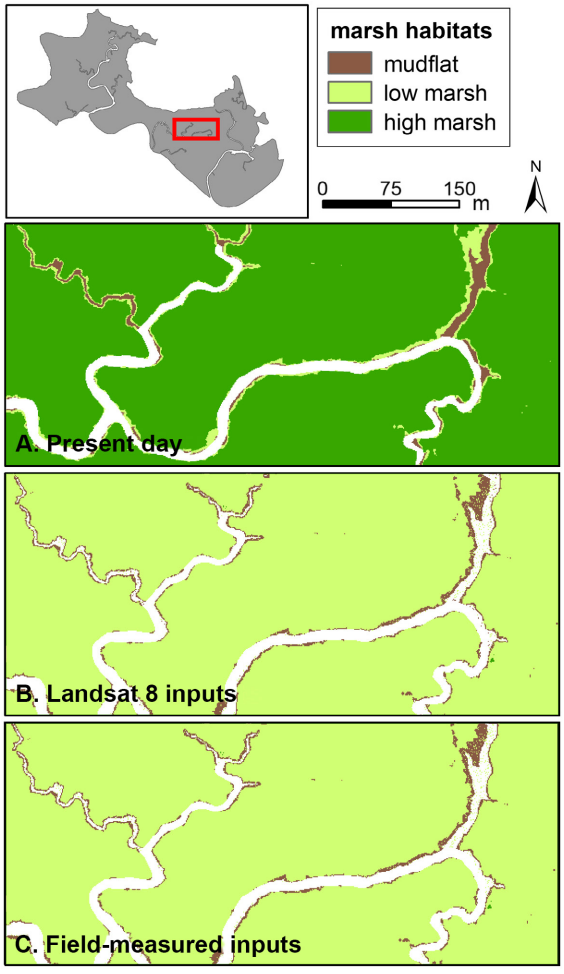

Fig. 9. (A) Present-day marsh habitat at Rush Ranch and comparison of Marsh Equilibrium Model projections of marsh habitat change based on (B) Landsat 8 derived inputs and (C) field-derived inputs for peak biomass and annual average suspended sediment concentration.

Compared with Landsat 8, the dynamic range of biomass predictions and overall accuracy was similar for the AVIRIS model. However, that AVIRIS image was collected early in the growing season, prior to peak biomass, so the estimated peak biomass was lower than the value required for the MEM. In the future, the planned HyspIRI hyperspectral satellite, with 30 m resolution and a 16-day return interval, will provide opportunity for improved biomass modeling at different phenological stages (Turpie et al. 2015). Average error in the WV2 model was similar to those of Landsat 8 and AVIRIS, reflecting other studies that demonstrated the utility of WV2 for biomass estimation (Mutanga et al. 2012, Byrd et al. 2014). However, the WV2 model generated the lowest estimate of peak biomass.

With a return interval of 16 d, we constructed an estimate of average annual SSC using 12 cloud-free Landsat 8 scenes from June 2013 to May 2014. While we had limited in situ samples to evaluate the Landsat 8 model, a time series of in situ SSC data derived from turbidity measurements at a continuous monitoring station showed the same seasonal trends as in the Landsat 8 imagery. To further test and validate the Landsat 8 SSC model, additional in situ SSC should be collected coincident with Landsat 8 overpasses.

The WV2 SSC model accuracy was similar to the Landsat 8 model (23% RMSE). With a high 2 m resolution, the WV2 imagery allowed for estimation of SSC in small channels present throughout tidal marshes. Although this satellite has a return interval of 1–2 d, the cost of commercial imagery could pose limitations for repeated acquisitions. PRISM has the narrow bands and high spatial resolution to accurately map SSC in small channels, and its accuracy was higher than the other sensors (16% RMSE). However, the costs of preparing and executing flight paths over the study site are likely to limit its temporal resolution.

In mapping SSC in Suisun Bay and its tidal channels, we found there to be significant influence from CDOM at red wavelengths (see Fichot et al. 2016). As tidal marshes are a main source for CDOM, extension of this application to other marsh sites will likely require sensors with NIR bands. Additionally, a remote sensing platform with bands in the SWIR can be useful for atmospheric correction over turbid waters (Vanhellemont and Ruddick 2015). The successor to WV2 (WorldView-3) possesses bands in NIR and the SWIR and has an improved resolution of 1.2 m. These features may make WorldView-3 an ideal sensor for the measurement of SSC in small marsh channels.

Spatial pattern and distribution of model inputs

All Landsat 8-based peak biomass values were located at the channel edge, and locations of peak biomass were randomly distributed across the Rush Ranch tidal marsh area (Fig. 3B). This distribution of peak biomass values across the model spatial extent and their consistent position low in the tidal frame provide confidence that the satellite-measured peak biomass value and the biomass/elevation growth response curve, a key parameter of MEM, represent conditions across the tidal marsh extent; therefore, MEM elevation projections should be applicable across the model domain. However, the response of vegetation to sea level could vary across a mosaic of marsh landscapes. Instead of a single growth response curve, there are a family of curves, each representing a different combination of variables that affect vegetation growth, such as salinity and sediment permeability (Morris et al. 2013). The choice of a different curve may be based on increased understanding of how drainage affects the shape of the curve, or how curves differ across plant communities. A cluster of peak biomass values may also indicate the need for a different growth curve for another portion of the marsh. In particular, invasive pepperweed, which can generate high biomass, grows across a wide range of elevations in the Rush Ranch marsh. An important next step should be to generate a growth response curve for this species to determine how it may affect marsh sustainability. Absent perfect knowledge, we use a single curve to represent the entire marsh.

The synoptic measurements of SSC with satellite data represent the first characterization of the spatial and temporal dynamics of this variable in the channel system surrounding Rush Ranch. Previous measurements of SSC were limited to a one month period at four stations within the marsh (Ferner et al., *in press*). This improved understanding of SSC baseline conditions greatly increases the capacity to address many questions related to the sustainability of this brackish marsh. With this information, we may develop more fine-tuned scenarios of change and test with greater accuracy the feedbacks between organic and inorganic inputs. In addition, the model estimate of annual average SSC, 30 mg/L, was well represented in the channels surrounding Rush Ranch, with 80% of Landsat-based values falling between 28 and 33 mg/L.

MEM sensitivity

In a comparison of field and remote sensing inputs, the low marsh and mudflat transition zone (80–140 cm NAVD88) was the most sensitive marsh region to the lower remote sensing values, with differences >10 cm after 100 yr (Fig. 7). These differences were associated with feedbacks between the peak biomass and SSC inputs. Alone, remote sensing peak biomass or SSC values used here were accurate enough to generate the same elevation forecasts as field-derived data, with differences <10 cm for all elevations except the lowest (80–90 cm NAVD88; Table 1, Byrd 2016).

Greater differences between biomass remote sensing estimates and their error terms produced more variation in elevation projections, earlier in the model run and across a greater elevation range (Fig. 8A, C). Feedbacks between peak biomass and SSC were also found when evaluating MEM response to the range of input values derived from remote sensing error (±RMSE).

Here, the RMSE BM-SSC run (Model run no. 10, Table 4, Fig. 8H) exhibited the greatest deviation from the remote sensing-estimated values, with a difference of 39 cm after 100 yr (Byrd 2016). Above an elevation of 160 cm, differences in this comparison dropped below 10 cm (Fig. 8H).

The interaction of biomass and SSC at the lower marsh transition may indicate the vulnerable nature of this zone to both organic and inorganic accretion processes, and especially biomass enhanced sediment deposition. However, the elevation at the marsh edge that exhibits the highest sensitivity to MEM inputs represents less than 3% of the marsh plain area (Fig. 7). Finally, remote sensing and field-based elevation projections produced the same maps of vegetation distributions at 100 yr (Fig. 8).

It is important to consider the drivers and effects of marsh erosion on marsh sustainability (Kirwan and Megonigal 2013). While MEM models accretion and not erosion processes, our results here show that MEM sensitivity at the marsh edge for this site, characterized by steep channel banks, would not significantly influence estimates of total marsh area loss due to changes in accretion. However, tidal marshes can be vulnerable to erosion, particularly when exposed to wave action. Wave action can make marshes unstable in the horizontal direction, even if resilient in the vertical direction (Fagherazzi et al. 2013). Marsh loss through marsh edge erosion occurs in many coastal environments, with loss rates ranging up to 3 m/yr (Fagherazzi et al. 2013). In these environments, accretion models such as MEM would be limited in their capacity to determine the fate of tidal marshes.

Implications for using remote sensing data

The results of our sensitivity analysis demonstrate the feasibility of running MEM or other newly emerging coastal forecasting models with remote sensing data. For example, remote sensing of SSC would inform a coupled model of marsh erosion and migration (Kirwan et al. 2016*b*), while remote sensing of biomass would provide biomass distributions for Hydro-MEM, which links a hydrodynamic model with MEM (Alizad et al. 2016). However, some limitations of using remote sensing data should be considered. Estimates of peak biomass are dependent on spatial scale; based on our surveys, the highest values were found infrequently at the 1-m^2 scale—12 plots of 368 exceeded 2000 g/m^2, while average peak biomass at the 30-m scale was substantially lower. We found that scaling biomass by FVC in mixed pixels allowed us to adequately estimate biomass using Landsat 8 data (16% RMSE) and obtain peak biomass values comparable to those measured in the field. In addition, the 1-m^2 plot with the highest biomass measured at 3021 g/m^2 and contained 90% cover of woody, invasive perennial pepperweed. Pepperweed was not included in the model of peak biomass, as its spectral signature varied significantly from other marsh vegetation. Pepperweed has become dominant in portions of Rush Ranch in recent years, and with its woody structure, it has potential for yielding high biomass. More research is needed on the influence of invasive species such as pepperweed on marsh sustainability.

One limitation to using Landsat 8 for estimating annual SSC is the inability to control for tidal stage at the time of image acquisition. Sediment concentrations measured at different times in the tidal cycle may serve as conflicting indicators of marsh vulnerability, with high concentrations at flood tides representing a stable marsh and high concentrations at ebb tides representing an eroding marsh (Ganju et al. 2015). Also turbidity levels (correlated with SSC) are higher at low tides in our study region (Fichot et al. 2016). Of the 12 scenes selected for calculation of our annual SSC value, six were collected during ebb tide. However, the resulting estimated value matched closely with SSC measured in the field (30 vs. 37 mg/L).

Also, determining SLR impact in the intertidal zone is highly dependent on the accuracy of the elevation data available for those areas. As shown in the sensitivity analysis, minor changes in elevation on the order of centimeters can drive key processes such as accretion (Gesch 2009), and so uncertainty in elevation data in coastal impact models can limit the accuracy of predictions and their usefulness for management and planning (Runting et al. 2013). Bare earth DEMs derived from lidar typically have high vertical error in tidal marshes, due to the interference of dense marsh vegetation with the lidar signal (Chassereau et al. 2011). Multiple approaches are being developed to correct this error. In particular, the use of vegetation-specific correction factors with real-time kinematic GPS and high-resolution

vegetation maps have been found to reduce RMSE in a Georgia salt marsh from 16 to 10 cm (Hladik and Alber 2012) and reduce RMSE from 21.2 to 9.8 cm in a San Francisco Bay salt marsh (McClure et al. 2016). With a vegetation-corrected lidar DEM, other key MEM variables should be derived with remote sensing data, including elevation of peak biomass and minimum and maximum elevations of marsh vegetation.

Applications for remote sensing-based forecasts of coastal habitats

Landscape-scale projections derived from improved understanding of baseline conditions will help coastal management that occurs across a region, both for natural resources and coastal communities. Regional projections of marsh habitat change can be analyzed with landscape metrics such as patch size, edge, and shape complexity to assess future fish utilization of habitats (Torio and Chmura 2015). Also, projections of salinity changes and habitat connectivity can be combined to assess future habitat suitability for bird species (Zhang and Gorelick 2014).

While not a biogeochemical model, the ecological processes modeled in MEM can generate forecasts of soil carbon sequestration. Scientists are currently testing approaches for accounting for carbon emissions and removals associated with wetland management according to 2013 IPCC Wetlands Supplement guidelines (IPCC 2014). Quality of reporting is measured from low (Tier 1) to high (Tier 3) depending upon data availability and analytical capacity. The integration of remote sensing data with MEM may be a feasible approach for moving to a Tier 3 GHG inventory of coastal wetlands.

In addition, tidal marshes have the potential to protect many flood-prone coastal populations mainly by reducing wave energy reaching the coastline (Burkett and Davidson 2012, Temmerman et al. 2013). The long-term sustainability of the use of tidal marshes for ecosystem-based coastal protection is limited by the capacity of tidal marshes to keep up with SLR through natural accretion of organic and mineral sediments (Temmerman et al. 2013). Areal extent of marshes may be one of the most important constraints to their use for coastal defense, and the space needed will increase with tidal range (Bouma et al. 2014). Regional models of marsh accretion parameterized with remote sensing data could have important applications for forecasting the continued role of tidal marshes for coastal flood protection.

Finally, an updated version of MEM will also increase the feasibility of its application at the landscape scale by simplifying its parameterization. In MEM 5.4, the model makes a bulk density calculation based on soil organic and inorganic matter concentrations and derived from first principles (Morris et al. 2016). Taking the approach that a sediment pedon, or 3D unit of soil, is a stack of annual cohorts equilibrated with rising sea level, the final bulk density and mass of a cohort after it has passed the root zone will equal the rate of vertical accretion.

Conclusion

Regional planning documents call for forecasts of tidal marsh elevation change to support climate change adaptation decisions, although models have limited use if data inputs are not representative across sites and landscapes. Using a synoptic view of key parameters provides greater certainty in those forecasts. The use of remote sensing with MEM should advance regional projections of tidal marsh vegetation change by better parameterizing MEM inputs spatially and accounting for the organic and inorganic feedbacks in marsh accretion, compared with other regional models. The ability to use remotely derived datasets—SSC, aboveground marsh plant biomass, as well as lidar DEMs—to run a marsh projection model points to more efficient and effective efforts to map coastal wetland responses across the vast U.S. coastline. Improved information from remote sensing data should increase the capacity for coastal models such as MEM to better support planning for coastal ecosystem services, including habitat, carbon sequestration, and coastal protection from flooding. Further, with fieldwork required to calibrate MEM performance limited to a dated soil core organic matter profile, this approach may be useful on globally remote regions as well.

Acknowledgments

We thank Lisa Schile for access to Rush Ranch data, DEM, and vegetation distribution models. We thank the Solano Land Trust for access to the Rush Ranch

tidal marsh site. We thank Michael Vasey for project support and for assistance with field data collection. We thank Thomas Parker for use of SFSU drying ovens and laboratory space. For field data collection and processing, we thank Bernhard Warzecha, Anna Deck, Lara Martin, and Rebecca Crowe. For aquatic remote sensing field and modeling support, we thank Brian Bergamaschi, Emmanuel Boss, and Adam McClure. For PRISM data, we thank Cedric Fichot, Michelle Gierach, David R. Thompson (atmospheric correction, georeferencing), and the JPL PRISM team. For AVIRIS data, we thank the NASA HyspIRI Preparatory Airborne Campaign and the JPL AVIRIS team. This research was funded by the NASA Applied Sciences Program in Ecological Forecasting for Conservation and Natural Resource Management (Grant no. NNH14AX16I), the U.S. Geological Survey Land Change Science Program, and an award under the Federal Coastal Zone Management Act, administered by the National Oceanic and Atmospheric Administration's Office for Coastal Management (to San Francisco State University). Any use of trade, firm, or product names is for descriptive purposes only and does not imply endorsement by the U.S. Government.

Literature Cited

Alizad, K., S. C. Hagen, J. T. Morris, P. Bacopoulos, M. V. Bilskie, J. F. Weishampel, and S. C. Medeiros. 2016. A coupled, two-dimensional hydrodynamic-marsh model with biological feedback. Ecological Modelling 327:29–43.

APHA [American Public Health Association]. 1975. Method 208 D. Total nonfilterable residue dried at 103–105°C (Total suspended matter) in standard methods for the examination of water and wastewater. Fourteenth edition. American Public Health Association, Washington, D.C., USA.

Batzer, D. P., and A. H. Baldwin, editors. 2012. Wetland habitats of North America: ecology and conservation concerns. University of California Press, Berkeley and Los Angeles, California, USA.

Bouma, T. J., et al. 2014. Identifying knowledge gaps hampering application of intertidal habitats in coastal protection: opportunities & steps to take. Coastal Engineering 87:147–157.

Burkett, V., and M. Davidson. 2012. Coastal impacts, adaptation, and vulnerabilities: a technical input to the 2013 National Climate Assessment. Island Press, Washington, D.C., USA.

Buskey, E. J., M. Bundy, M. C. Ferner, D. E. Porter, W. G. Reay, E. Smith, and D. Trueblood. 2015. System-wide monitoring program of the National Estuarine Research Reserve System: research and monitoring to address coastal management issues. Pages 392–415 *in* Y. Liu, H. Kerkering, and R. H. Weisberg, editors. Coastal ocean observing systems. Elsevier Inc., London, UK.

Byrd, K. B. 2016. Data release for journal article titled, Forecasting tidal marsh elevation and habitat change through fusion of Earth observations and a process model. U.S. Geological Survey data release. http://dx.doi.org/10.5066/F76M34Z1

Byrd, K. B., J. L. O'Connell, S. Di Tommaso, and M. Kelly. 2014. Evaluation of sensor types and environmental controls on mapping biomass of coastal marsh emergent vegetation. Remote Sensing of Environment 149:166–180.

Callaway, J. C., E. L. Borgnis, R. E. Turner, and C. S. Milan. 2012. Carbon sequestration and sediment accretion in San Francisco Bay tidal wetlands. Estuaries and Coasts 35:1163–1181.

CDFG [California Department of Fish and Game]. 2012. Vegetation map update for Suisun Marsh, Solano County, California. A report to the California Department of Water Resources. June 2012. Vegetation Classification and Mapping Program Biogeographic Data Branch, California Department of Fish & Game, Sacramento, California, USA.

Chassereau, J. E., J. M. Bell, and R. Torres. 2011. A comparison of GPS and lidar salt marsh DEMs. Earth Surface Processes and Landforms 36:1770–1775.

Chen, J., S. Gu, M. Shen, Y. Tang, and B. Matsushita. 2009. Estimating aboveground biomass of grassland having a high canopy cover: an exploratory analysis of *in situ* hyperspectral data. International Journal of Remote Sensing 30:6497–6517.

Church, J. A., et al. 2013. Sea level change. Pages 1137–1216 *in* T. F. Stocker, D. Qin, G.-K. Plattner, M. Tignor, S. K. Allen, J. Boschung, A. Nauels, Y. Xia, V. Bex, and P. M. Midgley, editors. Climate change 2013: the physical science basis. Contributions of Working Group I to the Fifth Assessment Report of the Intergovernmental Panel on Climate Change. Cambridge University Press, Cambridge, UK.

Clare, S., and I. F. Creed. 2014. Tracking wetland loss to improve evidence-based wetland policy learning and decision making. Wetlands Ecology and Management 22:235–245.

Costanza, R., F. H. Sklar, and M. L. White. 1990. Modeling coastal landscape dynamics. BioScience 40:91–107.

Craft, C., J. Clough, J. Ehman, S. Joye, R. Park, S. Pennings, H. Guo, and M. Machmuller. 2008. Forecasting the effects of accelerated sea-level rise on tidal marsh ecosystem services. Frontiers in Ecology and the Environment 7:73–78.

Doxaran, D., J. M. Froidefond, and P. Castaing. 2003. Remote sensing reflectance of turbid sediment-dominated waters. Reduction of sediment type

variations and changing illumination conditions effects using reflectance ratios. Applied Optics 42: 2623–2634.

Drexler, J. Z., C. S. de Fontaine, and T. A. Brown. 2009. Peat accretion histories during the past 6,000 years in marshes of the Sacramento-San Joaquin Delta of California, USA. Estuaries and Coasts 32:871–892.

Enright, C., S. D. Culberson, and J. R. Burau. 2013. Broad timescale forcing and geomorphic mediation of tidal marsh flow and temperature dynamics. Estuaries and Coasts 36:1319–1339.

ESRI Inc. 1999–2014. ArcGIS 10.2.2. ESRI Inc., Redlands, California, USA.

Fagherazzi, S., G. Mariotti, P. L. Wiberg, and K. J. McGlathery. 2013. Marsh collapse does not require sea level rise. Oceanography 26:70–77. http://dx.doi.org/10.5670/oceanog.2013.47

Fagherazzi, S., et al. 2012. Numerical models of salt marsh evolution: ecological, geomorphic, and climatic factors. Reviews of Geophysics 50:RG1002.

Ferner, M. C., et al. *In press*. Mud on the move: a protocol for sampling suspended sediment within tidal wetlands. Technical Report, NOAA National Estuarine Research Reserve, Tiburon, California, USA.

Fichot, C. G., B. D. Downing, B. A. Bergamaschi, L. Windham-Myers, M. Marvin-DiPasquale, D. R. Thompson, and M. M. Gierach. 2016. High-resolution remote sensing of water quality in the San Francisco Bay-Delta Estuary. Environmental Science & Technology 50:573–583.

Fleck, J. A., B. A. Bergamaschi, B. D. Downing, and P. Stumpner. 2012. A non-point source of contaminants to the estuarine food web: mobilized particles from the intertidal zone. U.S. Geological Survey California Water Science Center, Sacramento, California, USA.

Frohlich, C., and G. E. Shaw. 1980. New determination of Rayleigh scattering in the terrestrial atmosphere. Applied Optics 19:1773–1775.

Ganju, N. K., M. L. Kirwan, P. J. Dickhudt, G. R. Guntenspergen, D. R. Cahoon, and K. D. Kroeger. 2015. Sediment transport-based metrics of wetland stability. Geophysical Research Letters 42:7992–8000.

Geladi, P., and B. R. Kowalski. 1986. Partial least-squares regression: a tutorial. Analytica Chimica Acta 185:1–17.

Gesch, D. B. 2009. Analysis of lidar elevation data for improved identification and delineation of lands vulnerable to sea-level rise. Journal of Coastal Research Special Issue 53:49–58.

Getis, A., and J. K. Ord. 1992. The analysis of spatial association by use of distance statistics. Geographical Analysis 24:189–206.

Gitelson, A. A. 2004. Wide dynamic range vegetation index for remote quantification of biophysical characteristics of vegetation. Journal of Plant Physiology 161:165–173.

Goetz, S., and R. Dubayah. 2011. Advances in remote sensing technology and implications for measuring and monitoring forest carbon stocks and change. Carbon Management 2:231–244.

Gonzalez Trilla, G., P. Pratolongo, M. E. Beget, P. Kandus, J. Marcovecchio, and C. Di Bella. 2013. Relating biophysical parameters of coastal marshes to hyperspectral reflectance data in the Bahia Blanca Estuary, Argentina. Journal of Coastal Research 29:231–238.

Gordon, H. R., and M. Wang. 1994. Retrieval of water-leaving radiance and aerosol optical thickness over the oceans with SeaWiFS: a preliminary algorithm. Applied Optics 33:443–452.

Green, R. O., et al. 1998. Imaging spectroscopy and the airborne visible/infrared imaging spectrometer (AVIRIS). Remote Sensing of Environment 65: 227–248.

Grewell, B. J., P. R. Baye, and P. L. Fiedler. 2014. Shifting mosaics: vegetation of Suisun Marsh. Pages 65–102 *in* P. B. Moyle, A. D. Manfree, and P. L. Fiedler, editors. Suisun Marsh: ecological history and possible futures. University of California Press, Berkeley and Los Angeles, California, USA.

Gross, M. F., M. A. Hardisky, V. Klemas, and P. L. Wolf. 1987. Quantification of biomass of the marsh grass *Spartina alterniflora* loisel using Landsat Thematic Mapper imagery. Photogrammetric Engineering and Remote Sensing 53:1577–1583.

Hladik, C., and M. Alber. 2012. Accuracy assessment and correction of a LIDAR-derived salt marsh digital elevation model. Remote Sensing of Environment 121:224–235.

IPCC [Intergovernmental Panel on Climate Change]. 2014. Chapter 4. Coastal Wetlands. Pages 4.1–4.55 *in* T. Hiraishi, T. Krug, K. Tanabe, N. Srivastava, J. Baasansuren, M. Fukuda, and T. G. Troxler, editors. 2013 Supplement to the 2006 IPCC guidelines for national greenhouse gas inventories: wetlands. IPCC, Switzerland.

ITT Visual Information Solutions. 2013. ENVI user's guide version 5.1. ITT Visual Information Solutions, Boulder, Colorado, USA.

Jones, N. L., and S. G. Monismith. 2007. Measuring short-period wind waves in a tidally forced environment with a subsurface pressure gauge. Limnology and Oceanography: Methods 5:317–327.

Kirwan, M. L., and G. R. Guntenspergen. 2012. Feedbacks between inundation, root production, and shoot growth in a rapidly submerging brackish marsh. Journal of Ecology 100:764–770.

Kirwan, M. L., G. R. Guntenspergen, and J. T. Morris. 2009. Latitudinal trends in *Spartina alterniflora* productivity and the response of coastal marshes to global change. Global Change Biology 15:1982–1989.

Kirwan, M. L., and J. P. Megonigal. 2013. Tidal wetland stability in the face of human impacts and sea-level rise. Nature 504:53–60.

Kirwan, M. L., S. Temmerman, E. E. Skeehan, G. R. Guntenspergen, and S. Fagherazzi. 2016*a*. Overestimation of marsh vulnerability to sea level rise. Nature Climate Change 6:253–260.

Kirwan, M. L., D. C. Walters, W. G. Reay, and J. A. Carr. 2016*b*. Sea level driven marsh expansion in a coupled model of marsh erosion and migration. Geophysical Research Letters 43:4366–4373.

Klemas, V. 2013. Remote sensing of coastal wetland biomass: an overview. Journal of Coastal Research 29:1016–1028.

Knowles, N. 2010. Potential inundation due to rising sea levels in the San Francisco Bay Region. San Francisco Estuary and Watershed Science 8:1–19.

Langley, J. A., and J. P. Megonigal. 2012. Field-based radiometry to estimate tidal marsh plant growth in response to elevated CO_2 and nitrogen addition. Wetlands 32:571–578.

Lewis, D., S. Phinn, and L. Arroyo. 2013. Cost-effectiveness of seven approaches to map vegetation communities – a case study from Northern Australia's tropical savannas. Remote Sensing 5:377–414.

Loisel, H., J.-M. Nicolas, A. Sciandra, D. Stramski, and A. Poteau. 2006. Spectral dependency of optical backscattering by marine particles from satellite remote sensing of the global ocean. Journal of Geophysical Research: Oceans 111:C09024.

Lu, D. 2006. The potential and challenge of remote sensing-based biomass estimation. International Journal of Remote Sensing 27:1297–1328.

Martinez-Lopez, J., J. Martinez-Fernandez, B. Naimi, M. F. Carreno, and M. A. Esteve. 2015. An open-source spatio-dynamic wetland model of plant community responses to hydrological pressures. Ecological Modelling 306:326–333.

Matthews, M. W. 2011. A current review of empirical procedures of remote sensing in inland and near-coastal transitional waters. International Journal of Remote Sensing 32:6855–6899.

McClure, A., X. Liu, E. Hines, and M. C. Ferner. 2016. Evaluation of error reduction techniques on a LIDAR-derived salt marsh digital elevation model. Journal of Coastal Research 32:424–433.

McKee, K., and W. H. Patrick. 1988. The relationship of smooth cordgrass (*Spartina alterniflora*) to tidal datums: a review. Estuaries 11:143–151.

McLeod, E., G. L. Chmura, S. Bouillon, R. Salm, M. Björk, C. M. Duarte, C. E. Lovelock, W. H. Schlesinger, and B. R. Silliman. 2011. A blueprint for blue carbon: toward an improved understanding of the role of vegetated coastal habitats in sequestering CO_2. Frontiers in Ecology and the Environment 9:552–560.

Mevik, B. H., and H. R. Cederkvist. 2004. Mean squared error of prediction (MSEP) estimates for principal component regression (PCR) and partial least squares regression (PLSR). Journal of Chemometrics 18:422–429.

Mevik, B. H., and R. Wehrens. 2007. The pls package: principle component and partial least-squares regression in R. Journal of Statistical Software 18:1–24.

Miller, R. L., and R. Fujii. 2010. Plant community, primary productivity, and environmental conditions following wetland re-establishment in the Sacramento-San Joaquin Delta, California. Wetlands Ecology and Management 18:1–16.

Mishra, D. R., H. J. Cho, S. Ghosh, A. Fox, C. Downs, P. B. T. Merani, P. Kirui, N. Jackson, and S. Mishra. 2012. Post-spill state of the marsh: remote estimation of the ecological impact of the Gulf of Mexico oil spill on Louisiana Salt Marshes. Remote Sensing of Environment 118:176–185.

Morris, J. T. 2016. Marsh equilibrium theory. Pages 67–71 *in* M. Ainouche, editor. Proceeding of the 4th International Conference on Invasive Spartina, ICI-Spartina 2014, Université de Rennes, Rennes, France, July 7–10, 2014. Université de Rennes Press, Rennes, France.

Morris, J. T., and B. Haskin. 1990. A 5-yr record of aerial primary production and stand characteristics of *Spartina alterniflora*. Ecology 71:2209–2217.

Morris, J. T., P. V. Sundareshwar, C. T. Nietch, B. Kjerfve, and D. R. Cahoon. 2002. Responses of coastal wetlands to rising sea level. Ecology 83:2869–2877.

Morris, J. T., K. Sundberg, and C. S. Hopkinson. 2013. Salt marsh primary production and its responses to relative sea level and nutrients in estuaries at Plum Island, Massachusetts, and North Inlet, South Carolina, USA. Oceanography 26:78–84.

Morris, J. T., et al. 2016. Contributions of organic and inorganic matter to sediment volume and accretion in tidal wetlands at steady state. Earth's Future 4:110–121.

Motohka, T., K. N. Nasahara, H. Oguma, and S. Tsuchida. 2010. Applicability of green-red vegetation index for remote sensing of vegetation phenology. Remote Sensing 2:2369–2387.

Moyle, P. B., A. D. Manfree, and P. L. Fiedler, editors. 2014. Suisun Marsh: ecological history and possible futures. University of California Press, Berkeley and Los Angeles, California, USA.

Mutanga, O., E. Adam, and M. A. Cho. 2012. High density biomass estimation for wetland vegetation using WorldView-2 imagery and random forest regression

algorithm. International Journal of Applied Earth Observation and Geoinformation 18:399–406.

Nechad, B., K. G. Ruddick, and Y. Park. 2010. Calibration and validation of a generic multisensor algorithm for mapping of total suspended matter in turbid waters. Remote Sensing of Environment 114:854–866.

Neukermans, G., H. Loisel, X. Mériaux, R. Astoreca, and D. McKee. 2012. *In situ* variability of mass-specific beam attenuation and backscattering of marine particles with respect to particle size, density, and composition. Limnology and Oceanography 57:124–144.

NOAA Coastal Services Center. 2012. 2009–2011 California Coastal Conservancy Coastal LiDAR Project. Department of Commerce, National Oceanic and Atmospheric Administration, NOAA's Ocean Service Coastal Services Center, Charleston, South Carolina, USA.

Pettorelli, N., W. F. Laurance, T. G. O'Brien, M. Wegmann, H. Nagendra, and W. Turner. 2014. Satellite remote sensing for applied ecologists: opportunities and challenges. Journal of Applied Ecology 51:839–848.

Pickens, B. A., and S. L. King. 2014. Linking multitemporal satellite imagery to coastal wetland dynamics and bird distribution. Ecological Modelling 285:1–12.

Rocchio, J. 2005. North American arid west freshwater marsh ecological system ecological integrity assessment. Colorado Natural Heritage Program, Fort Collins, Colorado, USA.

Röttgers, R., D. McKee, and S. B. Woźniak. 2013. Evaluation of scatter corrections for ac-9 absorption measurements in coastal waters. Methods in Oceanography 7:21–39.

Ruddick, K. G., V. De Cauwer, Y.-J. Park, and G. Moore. 2006. Seaborne measurements of near infrared water-leaving reflectance: the similarity spectrum for turbid waters. Limnology and Oceanography 51:1167–1179.

Ruddick, K. G., F. Ovidio, and M. Rijkeboer. 2000. Atmospheric correction of SeaWiFs imagery for turbid coastal and inland waters. Applied Optics 39:897–912.

Runting, R. K., K. A. Wilson, and J. R. Rhodes. 2013. Does more mean less? The value of information for conservation planning under sea level rise. Global Change Biology 19:352–363.

SAS Institute Inc. 1989–2014. JMP® version 11. SAS Institute Inc., Cary, North Carolina, USA.

Schalles, J. F., C. M. Hladik, A. A. Lynes, and S. C. Pennings. 2013. Landscape estimates of habitat types, plant biomass, and invertebrate densities in a Georgia salt marsh. Oceanography 26:88–97.

Schile, L. M., J. C. Callaway, J. T. Morris, D. Stralberg, V. T. Parker, and M. Kelly. 2014. Modeling tidal marsh distribution with sea-level rise: evaluating the role of vegetation, sediment, and upland habitat in marsh resiliency. PLoS ONE 9:e88760.

Schile, L. M., J. C. Callaway, V. T. Parker, and M. C. Vasey. 2011. Salinity and inundation influence productivity of the halophytic plant *Sarcocornia pacifica*. Wetlands 31:1165–1174.

Serdyuchenko, A., V. Gorshelev, M. Weber, W. Chehade, and J. P. Burrows. 2014. High spectral resolution ozone absorption cross-sections – part 2: temperature dependence. Atmospheric Measurement Techniques 7:625–636.

Shepard, C. C., C. M. Crain, and M. W. Beck. 2011. The protective role of coastal marshes: a systematic review and meta-analysis. PLoS ONE 6:e27374.

Soil Survey Staff. 2009. Soil Survey Geographic (SSURGO) Databases for the conterminous United States. Natural Resources Conservation Service, United States Department of Agriculture. http://soildatamart.nrcs.usda.gov

Stanley, D. J., and A. G. Warne. 1994. Worldwide initiation of Holocene marine deltas by deceleration of sea-level rise. Science 265:228–231.

Stralberg, D., M. Brennan, J. C. Callaway, J. K. Wood, L. M. Schile, D. Jongsomjit, M. Kelly, V. T. Parker, and S. Crooks. 2011. Evaluating tidal marsh sustainability in the face of sea-level rise: a hybrid modeling approach applied to San Francisco Bay. PLoS ONE 6:e27388.

Swanson, K. M., J. Z. Drexler, D. H. Schoellhamer, K. M. Thorne, M. L. Casazza, C. T. Overton, J. C. Callaway, and J. Y. Takekawa. 2014. Wetland accretion rate model of ecosystem resilience (WARMER) and its application to habitat sustainability for endangered species in the San Francisco Estuary. Estuaries and Coasts 37:476–492.

Temmerman, S., M. B. De Vries, and T. J. Bouma. 2012. Coastal marsh die-off and reduced attenuation of coastal floods: a model analysis. Global and Planetary Change 92–93:267–274.

Temmerman, S., P. Meire, T. J. Bouma, P. M. J. Herman, T. Ysebaert, and H. J. De Vriend. 2013. Ecosystem-based coastal defence in the face of global change. Nature 504:79–83.

Thenkabail, P. S., E. A. Enclona, M. S. Ashton, and B. Van Der Meer. 2004. Accuracy assessments of hyperspectral waveband performance for vegetation analysis applications. Remote Sensing of Environment 91:354–376.

Thompson, D. R., B.-C. Gao, R. O. Green, D. A. Roberts, P. E. Dennison, and S. R. Lundeen. 2015. Atmospheric correction for global mapping spectroscopy: ATREM advances for the HyspIRI preparatory campaign. Remote Sensing of Environment 167:64–77.

Thorne, K., D. Elliott-Fisk, G. Wylie, W. Perry, and J. Takekawa. 2014. Importance of biogeomorphic and spatial properties in assessing a tidal salt marsh vulnerability to sea-level rise. Estuaries and Coasts 37:941–951.

Thorne, K. M., J. Y. Takekawa, and D. L. Elliott-Fisk. 2012. Ecological effects of climate change on salt marsh wildlife: a case study from a highly urbanized estuary. Journal of Coastal Research 28:1477–1487.

Thorne, K. M., et al. 2015. Collaborative decision-analytic framework to maximize resilience of tidal marshes to climate change. Ecology and Society 20:30.

Tompkins, E. L., R. Few, and K. Brown. 2008. Scenario-based stakeholder engagement: incorporating stakeholders preferences into coastal planning for climate change. Journal of Environmental Management 88:1580–1592.

Torio, D. D., and G. L. Chmura. 2015. Impacts of sea level rise on marsh as fish habitat. Estuaries and Coasts 38:1288–1303.

Tucker, C. J. 1977. Asymptotic nature of grass canopy spectral reflectance. Applied Optics 16:1151–1156.

Turpie, K. R., V. V. Klemas, K. Byrd, M. Kelly, and Y.-H. Jo. 2015. Prospective HyspIRI global observations of tidal wetlands. Remote Sensing of Environment 167:206–217.

USEPA [U.S. Environmental Protection Agency]. 1979. Method no. 160.2 (with slight modification), Methods for chemical analysis of water and wastes, Report No. EPA-600/4-79-020 March 1979. U.S. Environmental Protection Agency, Office of Research and Development, Cincinnati, Ohio, USA.

Vanhellemont, Q., and K. Ruddick. 2014. Turbid wakes associated with offshore wind turbines observed with Landsat 8. Remote Sensing of Environment 145:105–115.

Vanhellemont, Q., and K. Ruddick. 2015. Advantages of high quality SWIR bands for ocean colour processing: examples from Landsat-8. Remote Sensing of Environment 161:89–106.

Warner, J. C., D. H. Schoellhamer, C. A. Ruhl, and J. R. Burau. 2004. Floodtide pulses after low tides in shallow subembayments adjacent to deep channels. Estuarine, Coastal and Shelf Science 60:213–228.

Weston, N. 2014. Declining sediments and rising seas: an unfortunate convergence for tidal wetlands. Estuaries and Coasts 37:1–23.

Whitely Binder, L., et al. 2010. Preparing for climate change in Washington State. Climatic Change 102:351–376.

Zhang, H., and S. M. Gorelick. 2014. Coupled impacts of sea-level rise and tidal marsh restoration on endangered California clapper rail. Biological Conservation 172:89–100.

Zhang, M., S. L. Ustin, E. Rejmankova, and E. W. Sanderson. 1997. Monitoring Pacific Coast salt marshes using remote sensing. Ecological Applications 7:1039–1053.